Original articles

Particle method for segmentation of breast tumors in ultrasound images

N. Karunanayake[a], P. Aimmanee[a], W. Lohitvisate[b], S.S. Makhanov[a],*

[a] *School of Information and Computer Technology, Sirindhorn International Institute of Technology, Thammasat University, Thailand*
[b] *Department of Radiology, Thammasat University, Thailand*

Abstract

We propose a new segmentation method based on multiple walking particles (WP) bouncing from the image edges. The particles are able to segment objects characterized by deep concavities as narrow as one pixel and handle single or multiple objects characterized by a noisy background and broken boundaries ("weak edge", "boundary leakage"). The particles are designed to segment the image by permanently staying inside the object and repairing the boundaries where necessary. The proposed WP combine the advantages of the continuous diffusion models with the principles of multi-agent systems.

WP have been tested against recent active contours and the distance regularized level set method on a set of complex-shaped synthetic images and ultrasound (US) images of breast cancer (http://onlinemedicalimages.com). The method has also been compared with localizing region-based active contours, the fuzzy C-mean level set method, and morphological active contours. The WP are faster and more accurate for images characterized by low contrast, noise, broken boundaries, or boundary leakage. However, for good quality, simple shaped objects the WP work similarly to the conventional methods. There is still an important difference even in this case: the WP do not require initialization.

A video demo of the algorithm is at https://drive.google.com/drive/folders/1SlTphINKtdUwvdjjxiakFrwI2dDlIUAU

© 2019 International Association for Mathematics and Computers in Simulation (IMACS). Published by Elsevier B.V. All rights reserved.

Keywords: Segmentation of medical images; Ultrasound image processing; Particle method

1. Introduction

The paper proposes a new efficient algorithm for automatic segmentation of complex images. The algorithm is based on the active agents (AA) also known as walking particles. The method circumvents one of the most challenging problems — *initialization*, required by the majority of the segmentation algorithms. The second advantage is the ability of the algorithm to segment deep concavities as narrow as one pixel. The main competitors, deformable contour methods — often are unable to resolve such thin, curved and elongated parts ("fingers"). One of the main reasons is a lack of space to construct a suitable vector flow force to move the deformable contour inside the finger. In this case the contour has to work on the subpixel level which is a major technical difficulty. Finally, the proposed WP are able to repair broken edges appearing due to "weak edge"/"boundary leakage", using special repair particles.

---

* Corresponding author.
   E-mail address: makhanov@siit.tu.ac.th (S.S. Makhanov).

The idea of WP for edge detection has been proposed in [28]. However, this model employs "charged" particles which attach themselves to the edges. Therefore, particles of this type enhance the boundaries but they do not have any segmentation or noise reduction properties. Moreover, they still must be connected in order to outline the object of interest.

As opposed to that, the proposed WP bounce off the edges, which creates a totally different dynamics of the particles suitable for fast and accurate segmentation. In the case of a single object we consider two classes: blue particles indicating the object and red particles belonging to the outside area.

Note that the proposed model is totally different from evolutionary models, such as the genetic algorithms, ant colonies, swarm intelligence (fireflies or bird flocks) models, etc. The WP are simple i.e. they do not employ any selection, competition, or other intricate components of the bio-inspired AI models which slow down the computations. However, the WP communicate. They also can increase their strength and infect WP from another class turning them into their own kind.

In this sense, the proposed model can be associated with artificial life. Artificial life for edge detection was originally proposed in [31]. The model combines region growing with the AA scanning the gray level intensities of the image and leaving pheromones at the pixels (an idea similar to the ant colony model). However, the model is pixel-based. The agents interact not only with each other but with all neighboring pixels which slows down the computations. Further, the model has been verified only on a few images and was not compared with other segmentation techniques. Therefore, it is not clear whether it provides an efficient segmentation at least for some class of images. Furthermore, several pixel-based AA have been proposed characterized by different behavior such as communication, perception, tagging, reproduction, diffusion, disappearance, etc. (see [8,16,19,46,47,59]).

In [52] the authors introduce an artificial potential field, created around pixels of interest which allows the agents to be gathered around edges and noise regions. At the boundaries between the regions, the agents are in competition to align the pixels of the boundaries to their respective regions. The resulting alternative alignment of the boundary pixels preserves the region boundaries against erasing. Noise regions that are characterized by small sizes or by aberrant depths (outliers) prevent the agents from adapting. Clearly, the model is a variant of the charged particles [28], mentioned above.

A combination of a multi-agent system, a deformable model and an edge detector is proposed in [23]. The model includes the region and the edge agents constrained by the gray levels, statistical models of the brain structures and general knowledge about MRI brain scans. However, the model is complicated. It requires statistics, some priory information, and training. Besides, it is not clear, whether the model can be generalized to another type of images.

As opposed to the above AA pixel-based models our proposed algorithm is edge-based. In other words, the agents "live" inside the edge map rather than inside the gray level image. This makes the model much faster since it does not need to analyze the gray level in its neighborhood unless it hits the edge.

A simple set of rules governing the model is formulated in a few lines as follows:

- the WP bounce off the edges,
- if a particle hits the image boundary, most likely it is outside of the object (red particle),
- if a particle stays a long time without touching the image boundary, most likely it belongs to the object of interest or one of the objects (blue particle).

The proposed WP have been tested against adaptive diffusion flow ADF [72], a recent distance regularized level set evolution (DRLSE) [41,42], on a set of synthetic and real US images of breast cancer. The ADF and DRLSE were selected as the most prominent representatives of the active contours (AC) and the level set method (LSM). We also test WP against localizing region-based active contours (LAC) [35], LSM combined with FCM (LSFCM) [38], and morphological active contours (MAC) [51]. All the above reference methods have been supplemented by their authors with downloadable source codes that were used in this paper for testing as follows: ADF [1], DRLSE [2], LAC [3], MAC [24], and LSFCM [4]. Our numerical experiments show that the WP outperform the reference methods in the accuracy and are faster for a majority of the test images.

2. State of the art

Deformable models such as active contours and the level set methods have been "massively used as an edge-based segmentation method" and "extensively used for US images" (survey [14]). According to another survey published in 2018, deformable models are the most frequently used approach to breast ultrasound segmentation due to their

properties, providing smooth and accurate results [49,73]. Since our application area is the US medical images, we consider the deformable models as our main opponent.

In 1988, Kass et al. proposed the first parametric active contour (AC) [32]. The ACs and their numerous modifications are based on a continuous curve evolving inside the image under the impact of an external force. A contour, characterized by the tension and elasticity, grows or contracts inside the image, to attach itself to the boundary of the desired object. The contour must retain its continuity, avoid loops, and still be able to resolve deep concavities, boundary leakage [72], and pass the noise and artifacts. The external force moving the contour towards the objects is derived from the gradient of the corresponding edge map. The mathematical model is a parametric curve (snake) $S(l) \equiv (x(l), y(l))$ which satisfies

$$aS_{ll} + bS_{llll} + V = 0,$$

where l is the coordinate along S, the subscripts denote partial derivatives, a, b are weighting parameters to control the snake's tension and rigidity, and V is the vector field of the external force. Since the seminal work [32], ACs have been applied to many image processing problems including medical image segmentation. Extensions of the model are the gradient vector flow (GVF) [76] and the generalized gradient vector flow field (GGVF) [75]. These models utilize an additional system of parabolic equations to extend and smooth the original gradient vector field which could be very noisy and chaotic. One of the most popular is the gradient vector flow — GVF [76] obtained by solving the following system of partial derivative equations

$$V_t = \mu \nabla^2 V + (\nabla f - V)|\nabla f|,$$

where, f is the edge map, and μ is a calibration parameter.

Modifications of these ideas are the multidirectional GVF [64] and the non-linear diffusion [70]. The latest GVF-type models are Normal Gradient Vector Flow [29], Infinity Laplacian [25], Harmonic Gradient Vector Flow [68], Convolution Vector Flow [36], Dynamic Directional Gradient Vector Flow [13], Adaptive Diffusion Flow [72], Multi-Feature Gradient Vector Flow [61], Fractional Energy Snakes [58], Adaptive-scale Active Contours [10], region-based ACs employing similarity factors [55] and ACs based on probabilistic principles [22].

Level set method was proposed in 1998 by Osher and Sethian [56]. The segmentation contour is the zero-level set of a 3D dimensional level set function. In the simplest case, if the contour moves with the speed v_{LSM} the level set function φ satisfies

$$\frac{\partial \varphi}{\partial t} = v_{LSM}|\nabla \varphi|.$$

The method handles topological changes of multiple contours, i.e., their merging, splitting, and collapse.

The current state-of-art LSMs are categorized into edge-based [11,41,42,77] and region-based (Chan and Vese) models [9,12,39,54,67].

The region-based LSM produces good segmentation results when the object of interest is characterized by homogeneous intensity. However, the model is "very sensitive to initialization and easily gets stuck into local minima" [43], which is a major problem for the segmentation of complex medical images. A new framework for the region-based LSM [35] is based on localized contours capable of segmenting heterogeneous objects. The technique is versatile, to be used with a variety of modifications of the region-based contour energy, with the benefits of localization. An original approach called the Morphological Active Contour (MAC) [51] replaces the partial derivative equations (PDEs) required for the region-based and the edge-based approaches by repeated application of morphological operators over a binary embedding function. The numerical experiments confirm that the MACs are comparable to ACs obtained by PDEs, except for narrow and elongated structures in which MACs better fit the objects of interest.

Through stop functions, the edge-based LSM uses the gradient information to attach the contour curve to the object boundary. Since the gradient is used as the stopping criteria, the edge-based LSM segments the images without any limitations on the homogeneity of the objects of interest. A classic example of the edge-based LSM is the geodesic active contour model proposed by Caselles et al. [11]. The distance regularized level set evolution (DRLSE) method proposed by Li et al. [41,42] is one of the most popular edge-based LSMs. The method eliminates the need for reinitialization of the contour required by the preceding methods and thereby avoids initialization-induced numerical errors. The recent modifications are the Neuro LSM [15], Narrow Band Graph Partitioning LSM [78], and Local Regional Fitting LSM [43], LSM preserving the distance function [20] and LSM employing

a speed function based on saturation and lightness [48] (skin cancer images). The controlling parameters of the LSM estimated by a classic segmentation method, create hybrid schemes. A strong example is a combination of the fuzzy C-means clustering and LSM proposed in [38] for medical images. Intensity-texture driven LSM [53] and Hierarchical Level Set Evolution Protocol [79] should be also mentioned in this category.

However, noise is inevitably introduced into the gradient images (edge maps) through a variety of ways [45]. Therefore, the edge-based LSMs are sensitive to noise as well. The methods depend on preprocessing and edge detection techniques to generate the corresponding edge maps. The over segmented edge maps lead to a large amount of noise, whereas the under segmented maps create broken boundaries and boundary leakage [72].

Consequently, the ACs and LSMs are often unable to handle a weak edge. In other words, when an edge is less than ideal, such as being blurred or broken, the contour "leaks" outside the actual boundary.

In 2013 Wu et al. [72] propose a new adaptive diffusion flow (ADF), that establishes a joint framework between the GVF and the image restoration techniques. Although it shows a good performance at weak edges and deep concavities, the method is still sensitive to the initialization, topology changes, and especially to the parameters of the Gaussian smoothing embedded into the algorithm.

Resolving deep concavities is closely connected to the rigidity of the AC, defined explicitly or implicitly. If the rigidity is low, the contour can penetrate the concavity. However, it can be easily attracted by false boundaries and noise. Additionally, the external force must drive the contour inside the concavity. However, if the concavity is long, curved, and only a few pixels wide, generating such a force is virtually impossible. The contours often cannot resolve sharp (narrow) corners due to the inherent continuity of the AC and LSM.

A partial solution to this problem is the Segmented Snake [71] proposed in 1998 by Wong and colleagues. The snake is disassembled into segments, each called an "open snake". Every open snake evolves independently. Finally, the evolved segments are merged into a new snake. This type of snake requires a careful definition of the blowing force to prevent overshooting and a computationally hard merging procedure to re-assemble the open snakes back into a single contour. However, it is one of the first papers which introduces the idea of multiple semi-independent "agents" moving inside the object with the task of segmentation.

Furthermore, the accuracy and the computational time of the ACs and the LSMs depends on the initial positions of the contours (seeds). If the seeds are not initialized close to the boundaries of the desired object, the contour can attach itself to false boundaries created by noise and artifacts.

Consequently, there exists a variety of techniques to initialize the contour close to the boundary so that the contour is totally inside or outside the object. The successful initialization considerably improves the accuracy of the method [60]. A variety of these procedures is based on the analysis of the underlying vector force which moves the contour to the edge. The recent modifications are force field segmentation [40], center of divergence methods [69,74], quasi-automated initialization (QAI) by Tauber et al. [65,66], Poisson Inverse Gradient Vector Flow (PIG) [37], and trial snakes [34] for automatic initialization of the seeds for AC and LSM. Another type of initialization relies on gray levels and textures, to place the seed points inside the object [18,30,50]. Saliency and feature maps have been proposed in [62]. [21] suggests a special vector field to combine the GVF and the texture. A Chan–Vese type model is proposed in [44]. A number of research papers in medical image processing use a typical position and/or a shape of the segmented human organ (see, for instance, [7] and [33]). However, the initialization algorithms still are not entirely reliable. Their success depends on the position of the object, its complexity, number of objects, noise, contract and other characteristics of the segmentation task.

Bouncing WP applied to *initialization* of the ACs and the LSM have been proposed in [60]. However, the particles were used solely to detect the correct initialization seeds, to be subsequently used by classic segmentation methods such as AC and LSM. Therefore, the segmentation properties of the WP have not been fully recognized. In this paper, the particles are no longer used for the initialization but rather have been used as an independent segmentation tool. The particles outperform state-of-art ACs and LSMs for strong false-boundary noise, long narrow cavities, and broken boundaries.

In [52], the authors introduce an artificial potential field, created around the pixels of interest, which allows the agents to be gathered around edges and noise regions. At the boundaries between the regions, the agents are in competition to align the pixels of the boundaries to their respective regions. The resulting alternative alignment of the boundary pixels preserves the region boundaries against erasing. Noise regions that are characterized by small sizes or by aberrant depths (outliers) prevent the agents from adapting. Clearly, the model is a variant of the charged particles [28] mentioned above.

A combination of a multi-agent system, a deformable model, and an edge detector is proposed in [23]. The model includes the region and the edge agents constrained by the gray levels, statistical models of the brain structures, and general knowledge about the MRI brain scans. However, the model is very complicated and requires statistics, and some prior information and training. Besides, it is not clear, whether the model [23] can be generalized to other types of images.

As noted above the proposed bouncing WP differ from evolutionary algorithms, such as genetic algorithms, ant colonies, swarm intelligence (fireflies or bird flocks) models, etc. since they do not use any selection, mutation, competition, or other sophisticated components of the bio-inspired AI models. These operations slow down the computations whereas WP are not intelligent and are characterized by a very simple functionality, i.e., they bounce off the edges and infect particles from another class, turning them into their own class. This simplicity allows a fast execution combined with a high accuracy.

If we translate this idea into a continuous level, the model can be considered as a discrete analogy of a diffusion model [57] with impenetrable walls (edges). However, the continuous model (parabolic equations) allows the particles (temperature, pollutant, etc.) to pass even through the smallest openings in the boundary. As opposed to that, our discrete model defines special particles (repair balls) which can repair the boundary if it has openings. The combination of small walking particles, being able to penetrate the cavities, and balls which are able to repair the boundary (in cooperation with the small particles) is the main contribution of this paper. The second important feature is that the model does not require initialization. Finally, the proposed model is characterized by fast processing which outperforms many other methods.

3. Algorithm and test on synthetic images

Currently, the proposed algorithm has been designed for US images of breast cancer. However, it applies to other types of images without significant modifications. We introduce two versions of the algorithm. The first version is designed for objects with a well-defined continuous or almost continuous boundary, characterized by deep concavities (as narrow as 1 pixel) and distorted by noise. The second model applies to both, deep concavities and broken boundaries. The model employs "repair particles" (balls) designed to restore the broken parts of the boundaries, in cooperation with the regular particles. This section introduces the model and demonstrates it on a set of synthetic images subjected to different types and intensity of noise.

3.1. Model 1. Well-defined boundary

The model includes several interacting objects obeying a set of simple rules as follows.

3.1.1. Pixels and particles

Pixels are classified as edge pixels E_m, image boundary pixels B_m, and regular pixels R_m. An edge pixel E_m is characterized by the score s_m. The initial score is defined depending on how strong the edge is (edge map). The score of the regular and boundary pixels $s_m = 0$. Evolution of the score depends on the relative number of red and blue particles which hit the pixel (see detailed explanations below). By a "hit" we understand a position when the distance between the pixel and the particle is less than or equal to one pixel.

Regular particles P_k are characterized by:
1. Position $(x, y)_k$ (the position is not necessarily integer).
2. Velocity v_k (if the minimal thickness of the edge is one pixel, $|v_k| = 1$).

v_k is subject to random fluctuations as $v_k = v_{d,k} + v_{r,k}$, where $v_{d,k}$, $v_{r,k}$ are deterministic and random components of the velocity, $|v_{r,k}| \leq |v_{d,k}|$.
3. Color $c_k = b$ (blue) or $c_k = r$ (red). The two colors apply to the case of a single object: blue corresponds to the object and red to the outside area. However, the model can be easily generalized to the case of multiple objects.
4. The particles change their color depending on the position of the neighboring particles.
5. The size of a regular particle is equal to one pixel.

3.1.2. Interactions: Particle–Particle and Pixel–Particle

Define a discrete pseudo-time $i = 0, 1, 2, \ldots$. Define a neighborhood of a particle P_k as all particles inside a circle with the radius Δ and a center at P_k. Denote the number of particles of the opposite color in the neighborhood P_k by $N_o(P_k)$. Define a neighborhood of a pixel P'_m as all particles P_k inside a circle with the radius Δ and a center at P'_m. Denote the number of particles of the blue/red color in the neighborhood of P_k, P'_m by $N_{blue}(P_k)$, $N_{red}(P_k)$, $N_{red}(P'_m)$, and $N_{blue}(P'_m)$.

The color of a particle P_k evolves as follows:

1. At $i = 0$ all the particles are blue.

2. If a particle P_k hits an edge E_m, it bounces off in the (approximately) opposite direction, i.e., $v_{k,new} = -v_k + v_{r,k}$ (Fig. 1(a)).

3. If a particle P_k hits an image boundary pixel B_m, it bounces off and the color of the particle becomes red ($c_k = r$) (Fig. 1(a)).

4. A particle P_k interacts with other particles as follows:

If $N_o(P_k) \neq 0$, the algorithm decides whether P_k has been infected by the opposite color using a randomized sigma-function given by

$$f_\sigma(N_o, \alpha, \beta) = 2\left(\frac{1}{1 + e^{-\alpha N_o}} - \frac{1}{2}\right) + \beta \tilde{n},$$

where $\tilde{n} \in [0, 1]$ is a uniformly distributed pseudo-random number. If $f_\sigma > \delta'$, where δ' is the threshold, the particle changes its color to the opposite color (Fig. 1(b)). We call this event an infection and calculate the number of infections I_i at time i (Fig. 1(b)). $f_\sigma(N_o, \alpha, \beta)$ for $\alpha = 0.85$, $\beta = 0.75$, and $\delta' = 0.9$ are used in this model, as shown in Fig. 1(c).

There exists a number of extensions of the above. In particular, the color can be defined as a continuous variable being incremented or decremented depending on the neighborhood. The infection model can be modified as well. However, the presented basic version of the algorithm is fast and shows accurate results.

The **edge pixels** evolve as follows.

1. At $i = 0$, each edge point E_m is characterized by the score s_m, equal to the intensity of the corresponding edge map scaled to [0, 1].

2. At $i = i_{start}$, each edge point registers the number of hits sustained from the red and the blue particles, denoted by $H_{red}(E_m)$ and $H_{blue}(E_m)$, respectively.
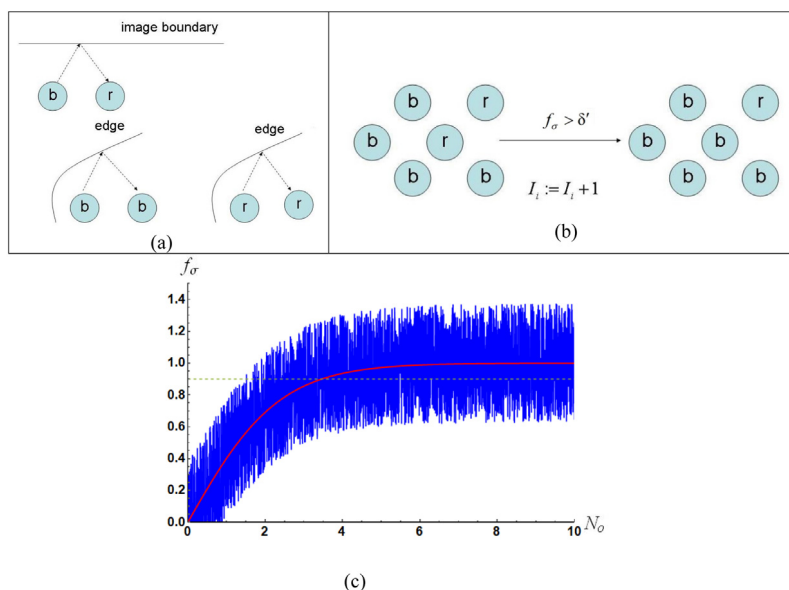

Fig. 1. Model 1 interactions (a) edge–particle, (b) particle–particle, (c) infection sigma-function.

3. If at time i, $H_{red}(E_m) \approx H_{blue}(E_m)$ the score is incremented: $s_m = s_m + \Delta s$ (Fig. 2(a))

4. If at time i, $H_{red}(E_m) \gg H_{blue}(E_m)$ or $H_{red}(E_m) \ll H_{blue}(E_m)$, the score is decremented: $s_m = s_m - \Delta s$ (Fig. 2(b))

5. If $s_m \leq 0$, the edge point E_m becomes a regular point R_m (Fig. 2(c)).

6. The stopping criterion is given by

$$\frac{\sum_m |s_m(i-1) - s_m(i)|}{m} \leq \delta_s \text{ and } I(i) \leq \Delta_I,$$

where $s_m(i)$ is the average score of the edge points given by

$$s_m(i) = \frac{1}{w} \sum_{k=i-w}^{i} s_k(i),$$

where w is a fixed time frame. The stopping criterion indicates that the edge points at time i are stable (do not change their score), and the particles are stable as well (do not change their color). In practice, the model is very reliable, so that we can set $\delta_s = \Delta_I = 0$.

Finally, the algorithm extracts the boundary of the object (the remaining edge) as well as the object region. To segment the object region, the model evaluates an average number ("density") of the blue particles per pixel P'_m during the time w given by

$$d_{blue}(P'_m) = \frac{1}{w} \sum_{k=i-w}^{i} N_{blue,i}(P'_m),$$

$d_{blue}(P'_m) > \varepsilon_{blue}$ indicates the object region. This threshold is selected close to zero. In practical calculations we use $\varepsilon_{blue} = N^*_{blue} 10^{-5}$, where N^*_{blue} is the number of blue particles.

3.2. Model 1. Tests on synthetic images

This section presents tests of the proposed WP against ADF snakes [72], LSM (DRLSE) [41,42], localizing region-based active contours (LAC) [35], LSM combined with FCM (LSFCM) [38], and the morphological active contours (MAC) [51]. The experiments are conducted on a set of 300 randomized synthetic images. Although we
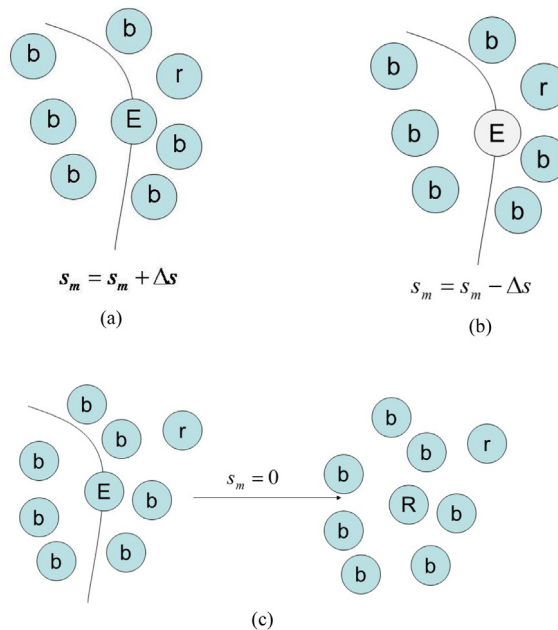

Fig. 2. Model 1 interactions (a) the edge score increases, (b) the edge score decreases. (c) the edge disappears.

consider objects resembling tumors in the US images, the test also shows the general efficiency and applicability of the WP to complex shaped objects.

The objects depicted in the images are characterized by an increasing level of complexity:

type 1: Round, smooth objects (Fig. 3(a))

type 2: Complex-shaped objects with smooth boundary (Fig. 3(b)–(d))

type 3: Objects characterized by long multiple concavities with corners (this type combined with a high SNR may produce edge maps with gaps about 2–3 pixels long (Fig. 3(e)).

The synthetic images are subjected to combinations of random and speckle noise (Fig. 4). We consider 5 levels of noise with the SNR approximately 9.0, 8.5, 8.0, 7.5 and 7.0 db and 20 different images of the above types. Therefore, the experiments include 300 images.

The convergence to the true boundary is registered when $\text{dist}_{H_2}(X, Y) \leq 3$, where

$$\text{dist}_{H_2}(X, Y) = \max(\text{average} \min_{\substack{a \in X \\ b \in Y}} \|a - b\|, \text{average} \min_{\substack{b \in Y \\ a \in X}} \|a - b\|)$$

is the average Hausdorff distance between the ground truth X and the generated contour Y.

It should be noted that all the above methods are edge based. Moreover, all of them are initialized inside the objects. Although the distortion outside the object may eventually affect the segmentation, most of the time, it is the internal false edges which prevent the model to attach itself to the true boundary, Therefore, we characterize the noise by comparing the binarized ground truth image and its distorted version as follows

$$\text{SNR}_O = 10 \log \frac{\sqrt{N_O}}{\|I - V_I\|},$$

where N_O the number of pixels inside the object, $I = (1, \ldots, 1)$ is a vector-version of the binarized image, V_I is a vector-version of the distorted image. $\dim I = \dim V_I = N_O$. Clearly, the quality of the edge map depends on complexity of the boundary and the SNR_O. For instance, noise with $\text{SNR}_O = 7.85$ applied to an object of type 1 preserves a smooth, continuous contour of the object, whereas type 3 subjected to approximately the same level of noise, $\text{SNR}_O = 7.91$, generates a low-quality edge map with gaps/weak boundaries (Fig. 3(e)).

The deformable contours are initialized automatically. The first method initializes the contour from a single point located at the "center" of the object. The second method uses a contour located in the "central part" of the object, covering approximately 50% of the area. Note that for complicated objects, the center of mass (or a centroid) often lies outside the object. Therefore, we employ a combination of the distance transform and thresholding, to offset the true boundary of the object (Fig. 5). Note that this works in favor of the preceding methods, since it offsets the ground truth (true contour) which is supposed to be unknown. As far as the proposed method is concerned, *it does not require initialization.* All methods are applied to the "raw" images without preprocessing. Fig. 6 shows typical results obtained for sample images of each type for $\text{SNR}_O \in [7.6, 8.2]$ (the third column in Tables 1–3 for initialization method 1 – Fig. 6(a) and initialization method 2- Fig. 6(b). Initialization free methods (LSFCM and WP) are illustrated in Fig. 6(c). Note that in case of WP the false boundary can be even attached to the true boundary. The particles "do not care" how strong the false boundary is or whether it connects to the true boundary.

The methods are compared in Tables 1–3. We recall that the tables show the percentage of the images which have been successfully segmented, i.e. $\text{dist}_{H_2}(X, Y) \leq 3$ pixels (the contours are close but not necessarily identical). In the tables A/B stands for: A — % of the images successfully segmented using initialization method 1, B — initialization method 2.

All conventional methods as well as WP work well on **type 1** when the $\text{SNR}_O \approx 8.5$ (the first column in Table 1). An 85% accuracy is achieved by DRLSE, MAC and LSFCM for $\text{SNR}_O \in [7.6, 8.0]$. However, the accuracy of WP is 100%. Further, WP show an accuracy of 85% for $\text{SNR}_O \in [7.2, 7.5]$ and 80% for a "critical" $\text{SNR}_O \approx 7.0$. On this level of noise contours of the objects are partially destroyed, creating gaps (the last column Table 1). In the latter case the competing methods fail except LSFCM — 40%.

The accuracy of the conventional methods (except LSFCM) applied to **type 2** becomes compromised for $\text{SNR}_O \in [8.5, 9.6]$ (Table 2). For $\text{SNR}_O \approx 7.5$ all the conventional methods fail, however the WP show an 85% accuracy for this case and a 60% accuracy for the "critical" $\text{SNR}_O \approx 7.0$ (Table 2).

Type 3 is the most difficult for segmentation since it includes multiple concavities. The boundary curve subjected to speckle and impulse noise is similar to the case of high frequency noise in Signal Processing. ADF and LAC show only a 60% accuracy for the $\text{SNR}_O \in [8.6, 10.0]$. Further, only WP survive the $\text{SNR}_O \in [7.8, 8.1]$ with a
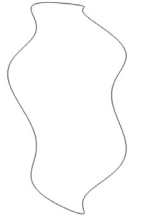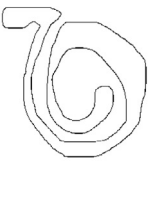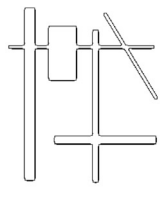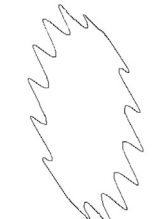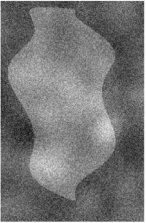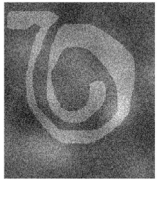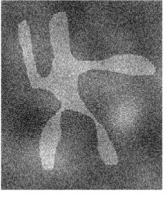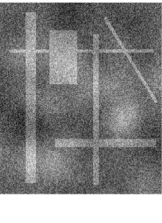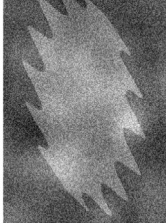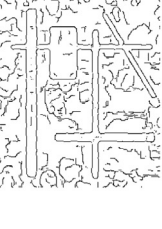
Ground truth					
Edge detected from the ground truth					
Strong noise with speckles					
SNR_O	SNR_O=7.85	SNR_O=7.95	SNR_O=9.0	SNR_O=9.0	SNR_O=7.9
Edge map of the distorted object					
Type	(a) type 1(smooth shape)	(b) type 2 complicated shape (spiral)	(c) type 2 complicated shape (star)	(d) type 2 complicated shape (intersection)	(e) type 3 (multiple concavities)

Fig. 3. Complexity of the synthetic images (examples).

(a) impulse noise   (b) speckle noise

Fig. 4. Artificial noise applied to synthetic objects.

| (a) ground truth (inverted) | (b) distance transform | (c) binarization, 1- centroid | (d) initialization. 1- centroid, 2- initial contour |

Fig. 5. Initialization of the deformable contour methods.

Table 1
Efficiency of the methods. Type 1 (gray columns indicate a presence of the boundary gaps $>= 2$ pixels).

Method/SNR_O	SNR_O range [8.2, 8.6]	SNR_O range[8.1, 8.2]	SNR_O range[7.6, 8.0]	SNR_O range[7.2, 7.5]	SNR_O range[6.8, 7.2]
DRLSE	100/100	100/100	85/60	60/40	20/0
ADF	100/100	80/65	40/20	0/0	0/0
MAC	100/100	100/100	85/60	45/20	0/0
LAC	100/80	80/65	40/20	0/0	0/0
LSFCM	100	100	85	60	40
WP	100	100	100	85	80

Table 2
Efficiency of the methods. Type 2.

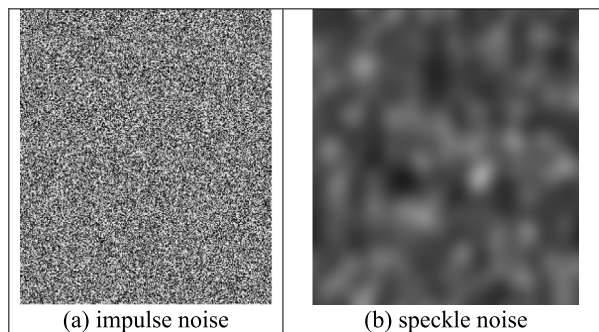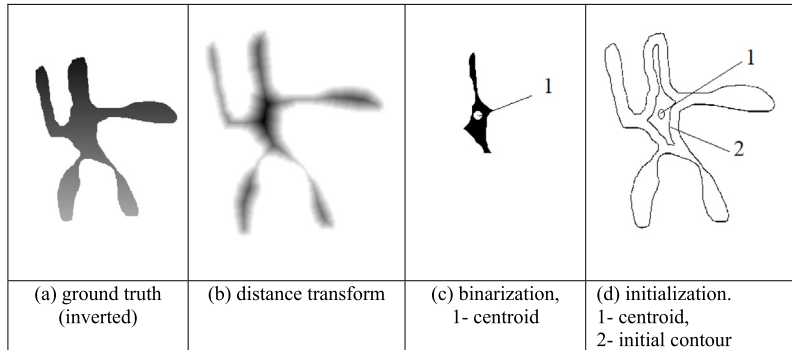| Method/SNR_O	SNR_O range[8.5, 9.6]	SNR_O range[8.2, 8.5]	SNR_O range[7.8, 8.2]	SNR_O range[7.5, 7.8]	SNR_O range[7.0, 7.4]
DRLSE	100/80	80/60	40/20	0/0	0/0
ADF	60/40	60/45	0/0	0/0	0/0
MAC	80/80	60/45	20/25	0/0	0/0
LAC	60/45	40/20	0/0	0/0	0/0
LSFCM	100	100	40	20	0
WP	100	100	100	85	60

satisfactory 80% accuracy. Finally, none of the methods, including WP, can process the images of type 3 subjected to the SNR_O lower that 7.5 (Table 3). The main reason of this failure is the multiple broken boundaries. Therefore, in Section 4 we introduce modified WP (Model 2) for treating these inaccuracies using repair particles.

The tests show a moderate sensitivity of the WP to a parameter α of the infection sigma-function (see Section 3.1.2, Fig. 1) and an increment Δs to modify the score of the edge pixels (Section 3.1.2). Table 4 shows an acceptable range of Δs and α obtained by testing 30 images of type 2 with the $SNR_O \in [7.5, 8.0]$. The table shows that small α (slow infection) leads to a decrease in the accuracy. In turn too large Δs (fast incrementing or decrementing the edge score) also decreases the accuracy. For instance for $\alpha = 0.35$ the accuracy drops below 80% and keeps decreasing as α decreases; for $\Delta s = 10^{-2}$ the accuracy is less than 80% and keeps decreasing as Δs increases. On the other hand, decreasing $\Delta s < 3 \cdot 10^{-3}$ does not impact the accuracy, although it increases the computational time (see Section 5.3, Experiment 4).

It may seem that Table 4 establishes that $\alpha > 1$ does not affect the accuracy of the model. However, it is not entirely correct. The sigma part of the infection function (Section 3.1.2, Fig. 1(c)) works only when the number of particles in a neighborhood of a candidate particle to be infected is relatively small. In turn, it means that the total number of particles is relatively small (the particle field is sparse). As an example, consider Table 5 which shows the accuracy of the method for a different number of particles versus the parameter α in $f_\sigma(N_o, \alpha, \beta)$ (Section 3.1.2). The experiments have been performed on images of type 2. The average $SNR_O \in [7.8, 8.2]$.
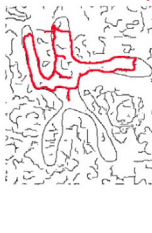
(a) initialization from a "central" point

Fig. 6. Sample results of segmentation.

Introduce $R_N = \frac{N_{\text{particles}}}{N_{\text{image pixels}}}$. For instance, for experiments presented in Table 4, $R_N = 1$, i.e. the number of particles is equal to the number of pixels. Table 4 shows that for $\alpha = 1$ and $\alpha = 1.1$ the accuracy is 100%

However, Table 5 reveals that if $R_N < 0.7$ (the initial number of the particles is less than 70% of the number of pixels) and the image is subjected to a considerable level of noise $\alpha > 1.0$ is not recommended.

Finally, it is hard, if not impossible, to analyze the efficiency of the model for a general image displaying an arbitrary object subjected to random noise. It is practical, to analyze the efficiency of the model for a particular

(b) initialization from the offset contour

Fig. 6. (*continued*).

type of images. Therefore, in Section 5 we compare WP and the selected above state of art methods applied to a particular but important type of medical images i.e. the US images of breast abnormalities.

4. Model 2. Broken boundary. Repair particles

To perform the segmentation of an object with broken boundaries, Model 1 has been enhanced by a special type of repair particles called "balls". The purpose of a ball is to find and repair the boundary gap. The ball is characterized by a variable size, which depends on the neighborhood of the ball. The ball obeys simple rules that are presented below.
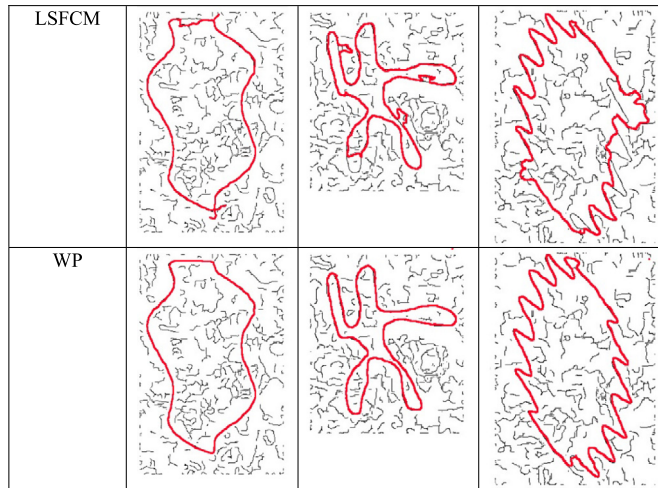
(c) initialization free methods

Fig. 6. (*continued*).

Table 3
Efficiency of the methods. Type 3.

Method/SNR_O	SNR_O range [8.6, 10.0]	SNR_O range [8.1-8.6]	SNR_O range [7.8, 8.1]	SNR_O range[7.4, 7.7]	SNR_O range[7.0, 7.3]
DRLSE	100/100	60/40	40/20	20/20	0/0
ADF	80/60	40/20	0/0	0/0	0/0
MAC	100/80	60/40	20/0	0/0	0/0
LAC	60/60	0/0	0/0	0/0	0/0
LSFCM	100	80	40	20	0
WP	100	100	80	45	25

Table 4
Sensitivity of Model 1 to α and Δs.

$\alpha/\Delta s$	$\alpha = 0.5$	$\alpha = 0.6$	$\alpha = 0.7$	$\alpha = 0.8$	$\alpha = 0.9$	$\alpha = 1.0$	$\alpha = 1.1$
$\Delta s = 3 \cdot 10^{-3}$	90	93	97	**100**	**100**	**100**	**100**
$\Delta s = 3.5 \cdot 10^{-3}$	90	93	97	**100**	**100**	**100**	**100**
$\Delta s = 4 \cdot 10^{-3}$	93	97	**100**	**100**	**100**	**100**	**100**
$\Delta s = 4.5 \cdot 10^{-3}$	93	97	**100**	**100**	**100**	**100**	**100**
$\Delta s = 5 \cdot 10^{-3}$	93	97	**100**	**100**	**100**	**100**	**100**
$\Delta s = 5.5 \cdot 10^{-3}$	93	97	**100**	**100**	**100**	**100**	**100**
$\Delta s = 6 \cdot 10^{-3}$	90	93	97	97	97	97	97
$\Delta s = 6.5 \cdot 10^{-3}$	90	93	97	97	97	97	97
$\Delta s = 7 \cdot 10^{-3}$	87	90	93	93	93	93	93

Table 5
Sensitivity of Model 1 to α and R_N.

R_N/α	$\alpha = 1.0$	$\alpha = 1.25$	$\alpha = 1.5$	$\alpha = 1.75$	$\alpha = 2.0$
1	**100**	97	93	93	93
0.9	97	97	93	93	93
0.8	97	97	93	90	90
0.7	93	93	93	87	87
0.6	93	90	90	83	82

4.1. End points and repair particles

Recall that the pixels are classified as an edge pixel E_m, image boundary pixel B_m, and a regular pixel R_m. Additionally, we introduce the **end points** (pixels). We thin the edge map so that the thickness of every edge is 1 pixel and define the end points Ω_m as pixels having only one neighboring edge point. The edge points that do not belong to $\Omega = \bigcup_m \Omega_m$ are called the true edge points.

Let us define the **repair particles** ("**balls**") as follows:

A ball B_k is a circle with the radius R_k, characterized by

1. Position $X_{B,k} = (x, y)_{B,k}$
2. Velocity $v_{B,k}$ (if the minimal thickness of the edge is one pixel then $|v_{B,k}| = 1$).
3. Neighborhood of B_k: a circle with the radius $R_{k,ext} = \alpha_k R_k$, $\alpha_k > 1$ denoted by $N_{ext}(B_k)$.
4. Status of ball B_k is defined as follows: if $F_k =$ true, the ball is considered to be "frozen", i.e., $v_{B,k} = 0$ (the ball found a gap and repaired the boundary). If $F_k =$ false, the ball is moving with the velocity $v_{B,k}$.
5. The union of balls having a non-empty intersection with B_k is denoted by $N_B(B_k)$.
6. Number of red (blue) particles in the neighborhood $N_{ext}(B_k)$ is denoted by $N_{red}(B_k)$ ($N_{blue}(B_k)$).

4.2. Ball–Ball, Ball–Particle, and Ball–Point Interactions

The balls are designed to repair a broken boundary. They move and change their size by the following rules.

1. Let us divide $N_{ext}(B_k)$ into N_S sectors and select the sectors with the smallest number of balls with probability p_1. The remaining sectors are selected with a probability $1 - p_1$. In the case of several candidates, the final sector is selected randomly with an equal probability for each candidate. The speed of the ball $v_{B,k}$ is assigned along the mid-direction of the sector (Fig. 7(a)). The ball changes its position by

$$X_{B,k} := X_{B,k} + v_{B,k}.$$

Rule 1 forces the ball into areas that still have not been explored. The practical value is $p_1 = 0.7$.

2. The available space is evaluated by the ball which grows or shrinks accordingly. The new size of the ball is defined by the maximum neighborhood $N_{ext}(B_k)$, which does not include edge points (Fig. 7).

3. The ball gets killed by the red particles, i.e., if the number of red particles in the neighborhood of B_k exceeds the threshold value $N_{red}(B_k) > N_{red,death}$, B_k gets erased and reinitialized inside the region with a high density of the blue particles. Therefore, the balls stay alive outside the object only for a short period of time and tend to be reborn inside the object.

4. If the ball B_k hits the boundary of the image, it dies and gets reborn, similar to Rule 3.

5. The ball ignores the edge points that are likely to be noise, i.e., their boundary score $s_m < s_{small}$ (Fig. 8).

6. The ball bounces off the edge points that are likely to be the boundary, i.e., their boundary score $s_m \geq s_{small}$ is large (Fig. 8(b)).

7. The ball "suspects" a gap if at time i, there are two end points $\Omega_{m,1}, \Omega_{m,2} \in B_k$ (Fig. 9).

8. If the ball suspects a gap, it scans the region ahead and behind, as shown in Fig. 9. The number of red particles ahead is denoted by $N_{red,ahead}(B_k)$, and the number of blue particles behind is denoted by $N_{blue,behind}(B_k)$, as shown in Fig. 9(a). If the number of red particles ahead is comparable with the number of blue particles behind, for instance, $\frac{N_{blue,behind}(B_k)}{N_{red,ahead}(B_k)} \approx 1$, the ball registers a gap. Next, the boundary from $\Omega_{m,1}$ to $\Omega_{m,2}$ is repaired, as shown in Fig. 9(b).

Remark 1. Not every ball that approaches the opening into a narrow concavity enters it, but sooner or later one of them will.

Remark 2. Not every ball that hits a gap will close it. Some balls pass the gap and are killed by the red particles. However, sooner or later, the gap will be closed.

Remark 3. The ball creates a temporary boundary. When the segmentation is finalized, these parts are replaced by cubic splines. Alternatively, this operation can be performed immediately, once the ball gets frozen.
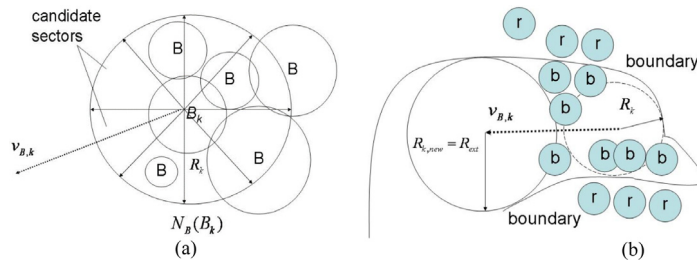
Fig. 7. (a) Selecting the next position of the ball, (b) selecting the size of the ball.
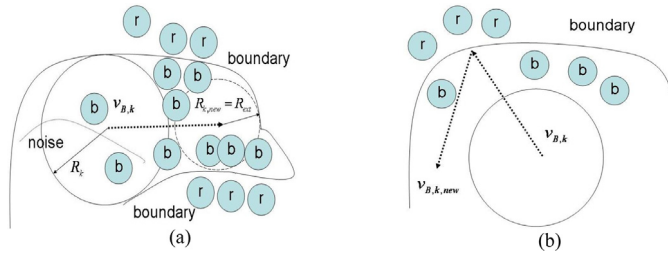
Fig. 8. (a) Ball ignores the noise, (b) ball bounces off a possible boundary.
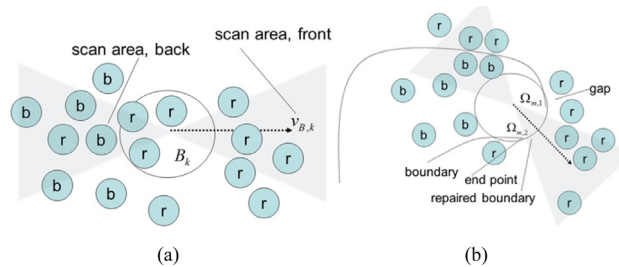
Fig. 9. (a) Ball's vision (b) ball closes the gap.

4.3. Tests on synthetic images with broken boundary

This section tests synthetic images similar to those introduced in Section 3.2 with an additional feature of the broken boundary. In case of boundary leakage [72], the edge detection routines often do not recognize parts of the boundary. This creates gaps. Experiments in Section 3.2 show that, most of the time, the success of deformable models as well as WP segmentation depends on the quality of the edge map i.e. the shape of the object, the presence of the boundary gaps and the intensity of the false boundaries. Therefore, in order to test this type of segmentation we characterize the edge maps (rather than the original images) by

(1) a ratio of the total length of the gaps to the length of the true contour $R_g = L_g/L_c$,
(2) a ratio of the maximum gap to the length of the true contour $R_{g,\max} = \max L_g/L_c$,
(3) a ratio of the total length of the false boundaries inside the object to the length of the true contour $R_f = L_f/L_c$.

Fig. 10 shows sample results obtained for 30 test objects 300×300 (see also Tables 6–8). The methods were tested on images of type 2 (Section 3.2) with the edge maps characterized by gaps and multiple false boundaries. The number repair particles for WP is 0.5% of the number of the image pixels i.e. 45 particles. All variables have been averaged over the 30 images. The boundary offset method was used for initialization with a 50% coverage of the object area (method-2, Section 3.2); recall that WP are initialization free.

Table 6 demonstrates a good performance of ADF (77%) and WP (97%) for $R_g = 0.06$, $R_{g,\max} = 0.025$, $R_f = 0.55$. Recall that these numbers mean that 6% of the actual boundary has been destroyed by the noise, the maximum gap is about 2.5% and the false boundaries as high as 55% of the true contour.

Sample images/Method	Distorted edge map	Ground truth	DRLSE	ADF	LSFCM	MAC	LAC	WP
Table 6 $R_g = 0.0913$ $R_{g,\max} = 0.246$ $R_f = 0.548$								
Table 7 $R_g = 0.128$ $R_{g,\max} = 0.044$ $R_f = 0.468$								
Table 8 $R_g = 0.147$ $R_{g,\max} = 0.0456$ $R_f = 0.829$								

Fig. 10. Sample results.

Table 6
WP vs. the reference methods: correctly segmented images (%). Varying R_g. $R_{g,\max} = 0.025$, $R_f = 0.55$.

R_g/Method	DRLSE	ADF	LSFCM	MAC	LAC	WP
$R_g = 0.063$	43.33	76.66	46.66	50	46.66	96.66
$R_g = 0.092$	30	70	36.66	40	40	90
$R_g = 0.117$	23.33	63.33	30	33.33	30	86.66
$R_g = 0.156$	0	46.66	0	23.33	0	83.33
$R_g = 0.215$	0	30	0	0	0	80

However, when R_g is increased, the accuracy of the ADF and other methods drops. When the total length of the gaps is 21% of the total contour, none of the competing methods generates a correct contour. However, WP still produces an 80% correct segmentation.

Table 7 shows the accuracy for varying $R_{g,\max}$. Note that the size of the maximum gap is one of the most important measures of the edge map quality. Indeed, if a continuous gap takes more than 20%–30% of the boundary, it is often impossible to restore the original object even for a human operator. Conversely, if the boundary includes many small gaps, even when their total length is 20% (Table 6) the WP are capable of efficient segmentation.

Table 7 shows that for $R_g = 0.12$, $R_f = 0.45$ and $R_{g,\max} = 0.023$ the ADF provides a reasonable accuracy of a 60% of the images. However, when $R_{g,\max} = 0.092$ (9%-gap), only WP produce almost 80% of correct segmentations. The other tested methods failed. The main reason of these failures is that the deformable models ignore large gaps and continue to expand until the contour attaches itself to a false boundary or reaches the boundary of the image.

Table 8 shows a sensitivity of the segmentation model to R_f — the density of the false boundaries inside the objects. The experiments have been performed for $R_g = 0.147$, $R_{g,\max} = 0.047$. The high density of the false boundaries becomes critical for the majority of the models. When $R_f = 0.84$ and $R_f = 1.27$ only WP show an acceptable performance of 80 and 70% respectively. However, for larger R_f the performance of WP also drops. The deformable models fail because they attach the contours to the false boundaries (all of these models fail for $R_f \geq 2$). In turn, the repair balls of the WP "get confused" and attach itself to the false gaps created by the false boundaries. As the result, the red particles penetrate the object, eventually kill all the blue particles and subsequently erase all the edges. However, even for $R_f = 3.21$ (the length of the false boundaries is over 3 times the length of the true contour) the WP model produces 60% of correct images. We conjecture that the efficiency of Model 2 can be further improved even for edge maps with a very poor quality.

Finally, the next section presents Model 2 applied to a particular but important case: the US images of breast abnormalities. The images include the above case of broken edges (weak boundaries).

Table 7
WP vs. the reference methods: correctly segmented images (%). Varying $R_{g,\max}$. $R_g = 0.12$, $R_f = 0.45$.

$R_{g,\max}$/Method	DRLSE	ADF	LSFCM	MAC	LAC	WP
$R_{g,\max} = 0.023$	23.33	60	26.66	33.33	30	93.33
$R_{g,\max} = 0.032$	20	4666	23.33	23.33	23.33	93.33
$R_{g,\max} = 0.045$	13.33	36.66	16.66	13.33	10	90
$R_{g,\max} = 0.061$	0	23.33	0	0	0	86.66
$R_{g,\max} = 0.073$	0	0	0	0	0	83.33
$R_{g,\max} = 0.092$	0	0	0	0	0	80

Table 8
WP vs. the reference methods: correctly segmented images (%). Varying R_f. $R_g = 0.147$, $R_{g,\max} = 0.047$.

R_f/Method	DRLSE	ADF	FCM	MAC	LAC	WP
$R_f = 0.84$	16	36.66	16.66	10	10	80
$R_f = 1.27$	13	30	10	0	0	70
$R_f = 2.04$	0	20	0	0	0	63.33
$R_f = 3.21$	0	0	0	0	0	60
$R_f = 3.52$	0	0	0	0	0	53.33

5. Segmentation of the abnormalities in the ultrasound images of breast cancer

To evaluate the performance of the method on the US images the following accuracy measures are used.

5.1. Contour based measures

- Hausdorff distance, given by $\text{dist}_{H_1}(X, Y) = \max\{\max_{a \in X} \min_{b \in Y} \|a - b\|, \max_{b \in Y} \min_{a \in X} \|a - b\|)$, where $\|\|$ denotes the Euclidian distance, X the ground truth contour, and Y the resulting contour
- average Hausdorff distance, given by $\text{dist}_{H_2}(X, Y) = \max(\max_{a \in X} \frac{1}{L_Y} \sum_{b \in Y} \|a - b\|, \max_{b \in Y} \frac{1}{L_X} \sum_{a \in X} \|a - b\|)$, where L_X, L_Y is the length of X and Y, respectively.
- relative Hausdorff distance, given by $\text{dist}'_{H_3}(X, Y) = \max\{\frac{\max_{a \in X} \min_{b \in Y} \|a - b\|}{L_X}, \frac{\max_{b \in Y} \min_{a \in X} \|a - b\|}{L_Y})$. Note that to avoid leading zeros, we consider $\text{dist}_{H_3}(X, Y) = \xi \text{dist}'_{H_3}(X, Y)$, where $\xi = 1000$ is a normalizing coefficient. This measure is similar to the so-called proportional distance [63].

5.2. Region based measures

- sensitivity: $SEN = \frac{TP}{TP+FN}$,
- specificity: $SPC = \frac{TN}{TN+FP}$,
- accuracy: $ACC = \frac{TP+TN}{TP+TN+FP+FN}$,
- Dice coefficient: $DICE = \frac{2TP}{2TP+FP+FN}$,
- Jaccard index: $JAC = \frac{TP}{TP+FP+FN}$,

where TP, TN, FP, and FN are the region-based true positive, true negative, false positive, and false negative. Note that the most popular region-based metrics in validating medical segmentations are the Dice coefficient and the Jaccard index [63]. The measures, including *TN*, *SPC*, and *ACC*, are sensitive to the size of the image. High values of *ACC* and *SPC* are possible even when the quality of segmentation is low. However, we include these measures for completeness.

5.3. Computational results

The algorithm has been tested on 400 US images of breast cancer obtained by a Philips iU22 ultrasound machine at the Department of Radiology, Thammasat University Hospital, Bangkok (http://onlinemedicalimages.com). The resolution ranges from 200×200 to 600×600 pixels. This section compares the results of WP with ADF, DRLSE,

LAC, LSFCM, and MAC in terms of the accuracy and the computational time. The US images have been divided into four types, characterized by the noise and the complexity of the boundary as follows:

Type 1: Clear round tumor (similar to type 1 in Section 3.2 with a low SNR_O)

Type 2: Round tumor distorted by noise, false boundaries, and gaps (similar to type 1 in Section 3.2 with a high SNR_O)

Type 3: Clear, complex shaped (speculated) tumor (similar to type 2 and type 3 in Section 3.2 with a low SNR_O)

Type 4: Complex shaped tumor distorted by noise, shadows, false boundaries, and gaps (similar to type 2 and 3 in Section 4.3 with a high SNR_O)

Fig. 11 illustrates the types.

The ground truth contours have been hand-drawn by an electronic pen on a Samsung Galaxy tablet by three leading radiologists of the Department of Radiology, Thammasat University. The final ground truth was obtained by the majority rule (two out of three). The numerical experiments show that the selected state-of-art methods are not suitable for arbitrary US images. When applied to weak edges (types 2 and 4), the models become unstable, i.e., sensitive to the positions of the gaps and configuration of the noise and artifacts. An automatic procedure to adapt control parameters of the conventional methods remains a challenging open problem. The proposed model shows a good performance for all types of images and requires minimal training.

Experiment 1. Sensitivity of the segmentation models applied to the US images

As an example, considering the segmentation by ADF [72] the proposed model requires seven basic parameters: the smoothness and tautness of the active contour, weighting functions similar to the classic GVF [64], and an additional weighting function to divide the image into edge regions, homogeneous regions, and transition regions. In our experiments, the above parameters have been taken from [1,72]. The model also requires the standard deviation of the Gaussian kernel σ_{ADF} to control the smoothness of the external force moving the snake towards the boundary. The second parameter κ "determines the contrast of the edges to be preserved and should be tuned for a particular application. If the edges are weak, κ should be small and vice versa" [72]. The recommended interval $\kappa \in [0.03, 0.12]$.

The bisection method was used to find to the best κ and σ_{ADF} using the seed values [1,72]. The scatter plot in Fig. 12 displays σ_{ADF} vs. κ, providing the best *DICE* coefficients for images of type 4. The area of the initial contours obtained by the offset method presented in Section 3.2 is approximately 70% and 30% of the object area. We denote these initializations by the subscripts 30 and 70.

The average $DICE_{30} = 0.452764$ and $DICE_{70} = 0.57047$. The low accuracy is combined with a large variation of the control parameters. For instance, $\sigma_{ADF,mean,30} = 2.442$ with standard deviation 0.58702, whereas $\kappa_{mean,30} = 0.065$ with standard deviation 0.028622. For the initial contours close to the boundary, we have
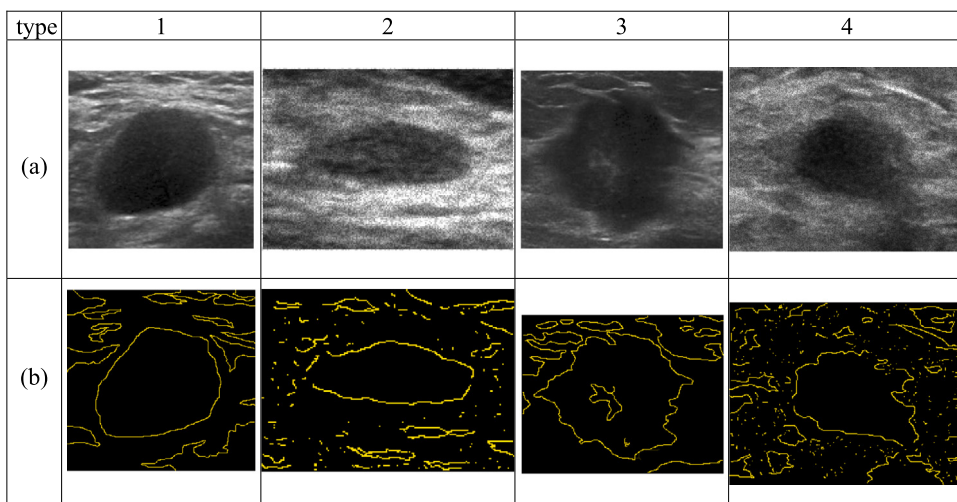
Fig. 11. Sample US images, (a) raw image, (b) edge map.
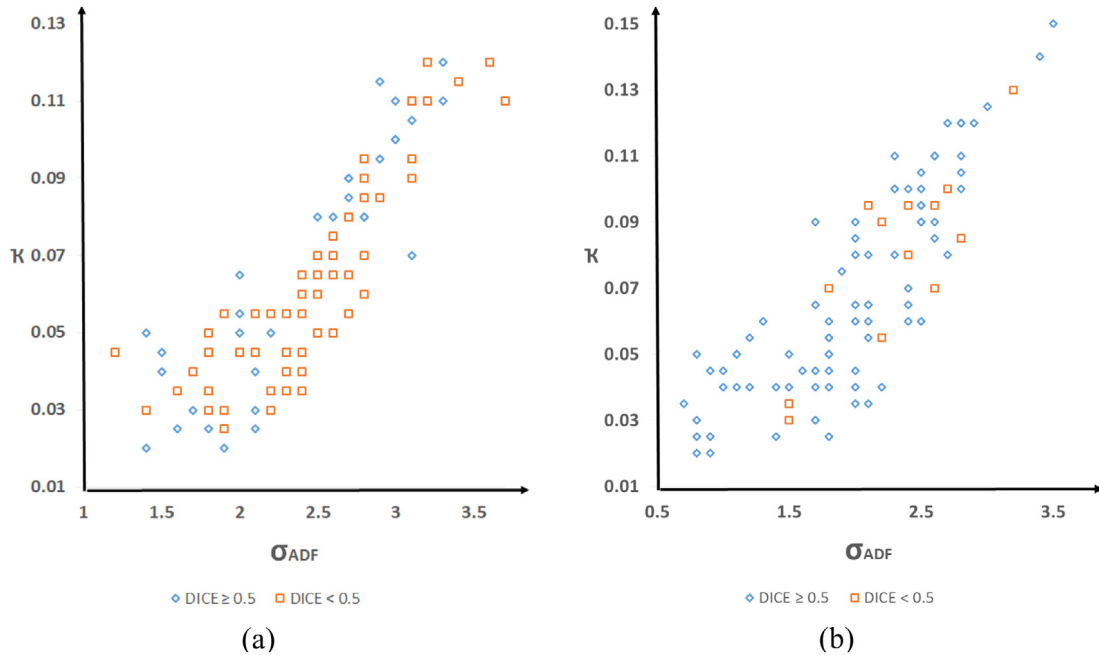
Fig. 12. Sensitivity of the ADF model to σ_{ADF} and κ (a) initialization: 30% of the object area, (b) initialization: 70% of the object area.

$\sigma_{\text{ADF,mean,70}} = 2.013$ with standard deviation 0.643484, and $\kappa_{\text{mean,70}} = 0.06957$ with standard deviation 0.031779. The experiment also reveals a large number of cases when the segmentation fails, namely, $DICE < 0.5$ for 60 and 13 images from 100, for 30 and 70% initial contours, respectively.

Finally, when fixed $\sigma_{\text{ADF}} = \sigma_{\text{ADF,mean}}$ and $\kappa = \kappa_{\text{mean}}$ are used to process the entire set of 100 images, the average *DICE* coefficients are 0.389571 and 0.496137 for 30% and 70% contours, respectively. The high sensitivity of the model, combined with more than a few failures (Figs. 13–14), does not allow to evaluate objectively the average accuracy for fixed σ_{ADF} and κ. The failed cases considerably reduce the average accuracy. However, excluding the failures creates unrealistic outcomes. Similar results are obtained for DRLSE, LAC, LSFCM, and MAC. The basic control parameters must be adjusted manually to exclude the failures and achieve a reasonable accuracy.

Table 9 shows the number of control parameters required for the tested methods N_{control}, and the number of parameters that (according to our experiments) do not need to be adjusted manually N_{fixed}.

Experiment 2. Testing WP against conventional models

The testing has been performed on 400 images divided into the above 4 types (Figs. 13 and 14). The edge maps are obtained by histogram equalization and Canny edge detection. The conventional methods have been trained to achieve a maximum accuracy in terms of the *DICE* coefficient *for every image individually*. The minimization is performed by bisection. *As opposed to that, WP were trained only once using 20 randomly selected images (5 of each type). The images were then excluded from the set, and the parameters of WP were fixed for the subsequent runs.*

Table 9
Control parameters of the segmentation methods.

Method	N_{control}	N_{fixed}	Reference
ADF	7	3	[72]
DRLSE	7	4	[42]
LAC	3	0	[35]
MAC	4	0	[51]
LSFCM	8	4	[38]
WP	7	7	

type	ground truth	DRLSE	ADF	LSFCM	MAC	LAC	WP
1							
2							
3							
4							
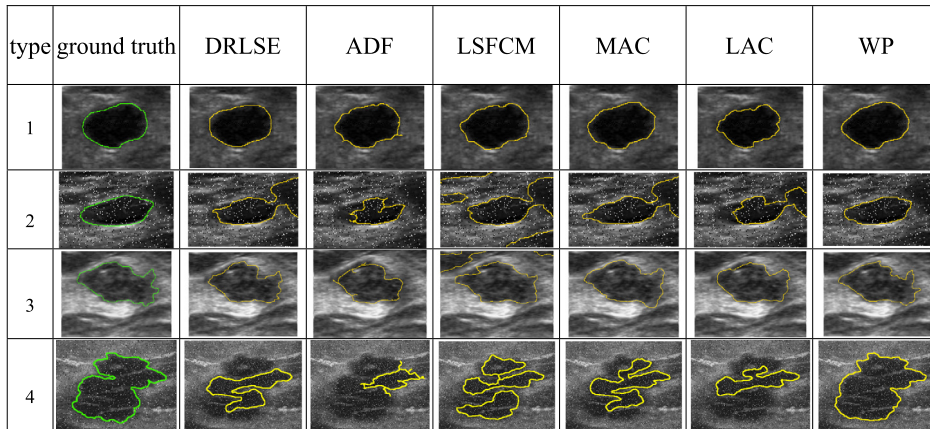
Fig. 13. Sample US images and segmentation results.
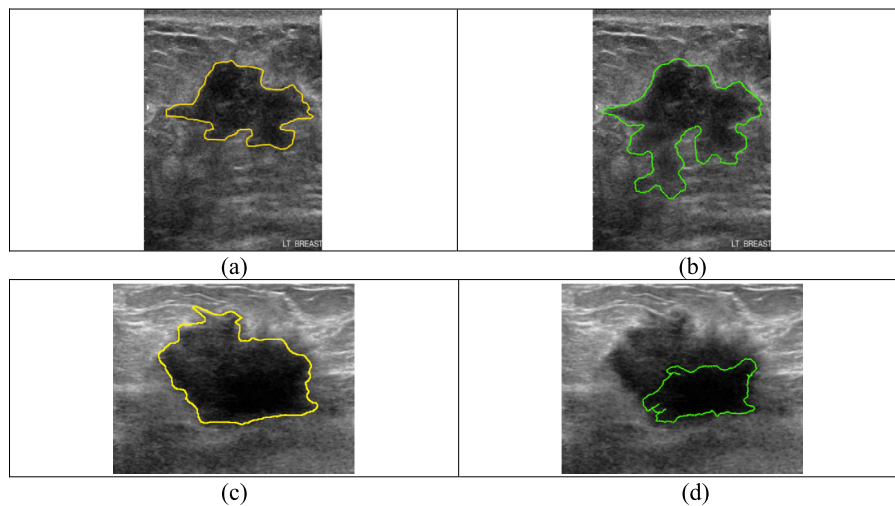
Fig. 14. Typical low accuracy segmentation using conventional methods. (a) and (c) ground truth images, (b) and (d) segmentation.

Therefore, the experiment has been designed so that the WP were in unfavorable conditions, whereas the conventional methods "knew" the ground truth in advance. However, WP outperform the five selected state-of-art methods even though they have been trained individually for every image. Tables 10–21 present the accuracy measures obtained by the experiments. The results have been averaged over the 100 images of each type.

The *DICE* coefficient is one of the most popular region-based measures in validating medical image segmentation along with the contour-based measures H_2 and H_3 that are based on the Hausdorff distance [52,63]. Several authors suggest that US image segmentation is acceptable only if $DICE \geq 0.8$ [26].

Applied to **type 1** with the initial contour covering 70% of the object, ADF, DRLSE, LAC, and MAC show an acceptable accuracy, i.e., $DICE_{70} \in [0.91, 0.95]$, $H_{2,70}[2.9, 4.5]$, $H_{3,70} \in [3.8, 6.5]$. The best results are $DICE_{\text{MAC},70} = 0.95$, $DICE_{\text{WP}} = 0.96$. When the initial contour covers 30% of the object, the average *DICE* coefficients of ADF and LAC drop to [0.8, 0.9]. LSFCM and WP (both initialization free) lead in this category with $DICE_{\text{LSFCM}} = 0.93$, $DICE_{\text{WP}} = 0.95$, $H_{2,\text{LSFCM}} = 3.76$, $H_{2,\text{WP}} = 2.39$, $H_{3,\text{LSFCM}} = 5.26$, and $H_{3,\text{WP}} = 3.42$ (Tables 10–12).

Since **type 2** is characterized by boundary gaps and an increased speckle noise, the accuracy of the conventional segmentation decreases. $DICE_{30}$ varies from 0.55 to 0.78. LSFCM is still efficient with $DICE_{\text{LSFCM}} = 0.82$.

Table 10
Type 1. Initial contour, covering 70% of the tumor.

| Model | Average Accuracy | | | | | | | |
| | Contour-Based | | | Region-Based | | | | |
	H_1	H_2	H_3	*SEN*	*SPE*	*ACC*	*JAC*	*DICE*
ADF	10.5672	4.5071	6.2129	88.0438	99.5122	97.1581	0.8532	0.9208
DRLSE	9.7989	3.2788	4.5009	94.2268	98.2876	97.5605	0.8831	0.9379
LAC	11.9565	4.5246	6.5259	86.2872	99.4918	96.7072	0.8411	0.9137
MAC	7.9739	2.8661	3.8671	94.5443	98.7989	98.0432	0.9049	0.9502

Table 11
Type 1. Initial contour, covering 30% of the tumor.

| Model | Average Accuracy | | | | | | | |
| | Contour-Based | | | Region-Based | | | | |
	H_1	H_2	H_3	*SEN*	*SPE*	*ACC*	*JAC*	*DICE*
ADF	17.7833	11.7726	15.5365	66.9026	99.9993	94.1512	0.6588	0.7943
DRLSE	13.2327	6.3870	8.5679	80.8351	99.5180	96.0648	0.7908	0.8832
LAC	18.2280	11.8023	16.7818	64.6513	99.9702	92.8986	0.6332	0.7754
MAC	9.4187	4.6210	6.5742	86.0097	99.4840	96.9055	0.8447	0.9158

Table 12
Type 1. Methods that do not require initialization.

| Model | Average Accuracy | | | | | | | |
| | Contour-Based | | | Region-Based | | | | |
	H_1	H_2	H_3	*SEN*	*SPE*	*ACC*	*JAC*	*DICE*
LSFCM	9.0640	3.7614	5.2618	93.7939	98.2990	97.2225	0.8713	0.9312
WP	**7.8999**	**2.3887**	**3.4209**	**95.0731**	**99.1483**	**98..3922**	**0.9207**	**0.9587**

Table 13
Type 2. Initial contour, covering 70% of the tumor.

| Model | Average Accuracy | | | | | | | |
| | Contour-Based | | | Region-Based | | | | |
	H_1	H_2	H_3	*SEN*	*SPE*	*ACC*	*JAC*	*DICE*
ADF	16.5209	9.8341	5.1386	74.8044	97.1355	93.8723	0.6403	0.7807
DRLSE	17.9824	7.5189	6.5851	78.5712	95.9013	93.3838	0.6565	0.7926
LAC	20.9016	8.8837	10.6924	69.6766	97.3795	93.3244	0.6137	0.7607
MAC	19.2318	7.2492	8.1076	76.2363	97.2674	94.2349	0.6621	0.7967

Table 14
Type 2. Initial contour, covering 30% of the tumor.

| Model | Average Accuracy | | | | | | | |
| | Contour-Based | | | Region-Based | | | | |
	H_1	H_2	H_3	*SEN*	*SPE*	*ACC*	*JAC*	*DICE*
ADF	19.9616	13.1840	10.8760	56.7334	98.9966	92.7514	0.5307	0.6934
DRLSE	17.8858	8.8747	8.9947	68.4160	97.2351	92.9840	0.5586	0.7618
LAC	23.1388	19.1014	18.8110	40.0583	99.2992	90.6725	0.3868	0.5578
MAC	17.9855	8.7845	9.9382	69.6859	98.4852	94.3151	0.6442	0.7836

However, the accuracy of WP practically does not change $DICE_{WP} = 0.9$. It should be noted that $H_{2,LSFCM} = 5.94$, whereas $H_{2,WP} = 4.22$ (better by 30%, see Tables 13–15).

Table 15
Type 2. Methods that do not require initialization.

| Model | Average Accuracy | | | | | | | |
| | Contour-Based | | | Region-Based | | | | |
	H_1	H_2	H_3	SEN	SPE	ACC	JAC	DICE
LSFCM	15.7239	5.9397	6.7673	80.2875	97.3645	94.9245	0.7071	0.8284
WP	10.8448	4.2243	3.9409	90.0987	99.1215	97.9079	0.8228	0.9028

Table 16
Type 3. Initial contour, covering 70% of the tumor.

| Model | Average Accuracy | | | | | | | |
| | Contour-Based | | | Region-Based | | | | |
	H_1	H_2	H_3	SEN	SPE	ACC	JAC	DICE
ADF	22.0103	6.3484	5.3127	82.0904	99.4713	95.0371	0.8034	0.8910
DRLSE	15.2662	4.7134	4.7998	85.8530	98.0314	95.7876	0.8300	0.9071
LAC	21.2659	7.5478	7.6901	78.6952	98.7463	94.0792	0.7654	0.8671
MAC	17.7054	4.8198	5.6575	85.5085	98.5413	95.2896	0.8152	0.8982

Table 17
Type 3. Initial contour, covering 30% of the tumor.

| Model | Average Accuracy | | | | | | | |
| | Contour-Based | | | Region-Based | | | | |
	H_1	H_2	H_3	SEN	SPE	ACC	JAC	DICE
ADF	28.5167	12.0929	15.2697	63.1033	99.9305	90.8481	0.6288	0.7721
DRLSE	23.7158	7.5415	8.2637	77.8543	98.9704	93.7601	0.7553	0.8606
LAC	29.8182	13.6566	22.8816	58.5958	99.8166	89.6652	0.5829	0.7365
MAC	19.8523	7.6024	7.3225	77.7239	98.8348	93.7303	0.7530	0.8591

Table 18
Type 3. Methods that do not require initialization.

| Model | Average Accuracy | | | | | | | |
| | Contour-Based | | | Region-Based | | | | |
	H_1	H_2	H_3	SEN	SPE	ACC	JAC	DICE
LSFCM	19.5676	4.9054	6.5271	84.9496	97.7873	94.8125	0.7940	0.8852
WP	11.8827	3.8968	2.3935	90.1232	99.1759	96.8515	0.8580	0.9236

Table 19
Type 4. Initial contour, covering 70% of the tumor.

| Model | Average Accuracy | | | | | | | |
| | Contour-Based | | | Region-Based | | | | |
	H_1	H_2	H_3	SEN	SPE	ACC	JAC	DICE
ADF	27.6170	13.9640	11.5167	56.0546	96.9520	86.4405	0.5107	0.6761
DRLSE	24.4198	12.0138	10.1526	63.3563	97.3495	89.9214	0.5700	0.7261
LAC	32.9986	14.0841	15.3515	58.5032	95.7018	86.6652	0.5202	0.6844
MAC	29.6982	10.0083	8.7168	70.5520	95.1644	89.3711	0.6029	0.7523

Type 3 includes irregular shapes but does not include boundary gaps. In this case, the performance of the competing methods improves (Tables 16–18). $DICE_{70}$ is 0.86–0.88, and $DICE_{30}$ is 0.7–0.88. However, WP also improves, producing $DICE_{WP} = 0.92$. The state-of-art methods are efficient in the case of corners and concavities when the contour is initialized close to the boundary. Nevertheless, H_2 and H_3 show the clear advantage of WP:

Table 20

Type 4. Initial contour, covering 30% of the tumor.

Model	Average Accuracy							
	Contour-Based			**Region-Based**				
	H_1	H_2	H_3	*SEN*	*SPE*	*ACC*	*JAC*	*DICE*
ADF	26.7855	19.9450	17.3886	41.0286	97.2018	83.8750	0.3820	0.5528
DRLSE	22.5179	13.2985	12.8876	56.8326	98.8969	88.8743	0.5526	0.7118
LAC	31.5821	21.4970	21.7853	34.0998	97.7177	82.9489	0.3237	0.4891
MAC	25.1190	12.2510	11.0421	62.1253	94.9954	87.0273	0.5216	0.6856

Table 21

Type 4. Methods that do not require initialization.

Model	Average Accuracy							
	Contour-Based			Region-Based				
	H_1	H_2	H_3	*SEN*	*SPE*	*ACC*	*JAC*	*DICE*
LSFCM	18.0830	9.6504	8.4912	72.2273	97.3944	91.7876	0.6635	0.7977
WP	13.3078	5.1276	5.9144	83.2103	98.4085	94.8266	0.8283	0.9061

$H_{2,WP} = 3.89$, $H_{2,LSFCM} = 4.94$ (the best for the conventional methods), whereas $H_{2,LAC,30} = 13.6566$ (the worst). $H_{3,WP} = 2.39$, $H_{2,LSFCM} = 6.52$ (the best for the conventional methods), whereas $H_{3,LAC,30} = 22.88$ (the worst).

Our test on the most challenging **type 4** shows *DICE* is 0.49–0.72 for the preceding methods except LSFCM, which remains relatively accurate, i.e., $DICE = 0.8$ (Tables 19–21). However, $DICE_{WP} = 0.91$. Moreover, $H_{2,WP} = 5.12$, whereas $H_{2,LSFCM} = 9.65$ (the best for the conventional methods). Note that H_2 for the other conventional methods ranges from 13.30 to 21.5 (low accuracy). Further, $H_{3,WP} = 3.94$ but $H_{3,LSFCM} = 8.59$ (the best for the conventional methods). H_3 for the other conventional methods ranges from 11.00 to 21.79. Therefore, $H_{2,WP}$ is almost two-fold better than the best conventional segmentation, and four-fold better than the worst result. In turn, $H_{3,WP}$ is more than two-fold better than the best conventional segmentation and five-fold better than the worst result. Recall that the conventional methods (including LSFCM) work in favorable settings when they "know" the ground truth, whereas WP is based on 20 training images. Note that $DICE_{ADF,30} = 0.67$ is slightly higher than in Experiment 1 since Experiment 2 employs an adaptive Canny edge map.

Finally, the experiments on a large number of US images (such as 400) with automatic initialization hold the greatest interest for medical image processing. A survey [27] cites a threshold-based segmentation method [26] applied to 400 US images. Multifractal processing combined with isotropic Gaussian smoothing has been tested on 360 US images in [26]. However, in both cases, the techniques use either a manually selected seed or a number of assumptions related to the position and the size of the tumor.

A variety of recent papers present general segmentation techniques applicable to a small series of $10 \sim 20$ US images. There are many downloadable programs with examples [5,6,17]. However, US images that are characterized by a variety of distortions are still hard to process. When their number reaches several hundred, almost every program requires a manual adjustment. Otherwise, it fails on a substantial number of samples.

Therefore, apart from testing the proposed new techniques, Experiment 2 is an interesting application of the state-of-art methods to a large series of the US images.

Experiment 3. Impact of edge detection.

The edge maps in Experiment 2 are obtained by histogram equalization and Canny edge detection with automatic thresholds and Gaussian smoothing characterized by standard deviation σ. Let us analyze the impact of the edge detection on the accuracy of the above segmentation methods.

Consider type 4. Let us train σ on 25 randomly selected images to maximize the average *DICE* coefficient. Note that rather than minimizing *DICE* for each image individually (as in Experiment 2), we consider minimization *for the entire set of 25 images.* Tables 22–23 display the results. The second column shows σ_{best} for the tested methods. The best *DICE* coefficient for the method appears on the diagonal (bold face). For instance, in Table 22 $\sigma_{ADF,best} = 3.96765$ and the corresponding $DICE_{ADF,70} = 0.6273$. The cells outside the diagonal show the *DICE*
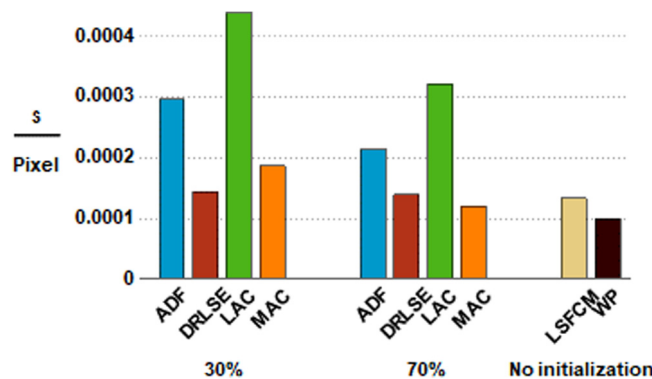
Table 22
$DICE_{70}$ for the tested methods for varying Gaussian smoothing. US images type 4.

Model	σ_{best}	Average $DICE$, WP	Average $DICE$, ADF	Average $DICE$, DRLSE	Average $DICE$, LAC	Average $DICE$, MAC	Average $DICE$, LSFCM
WP	2.2269	**0.8882**	0.5742	0.6187	0.6198	0.6918	0.7475
ADF	3.9765	0.7203	**0.6273**	0.3443	0.5786	0.6024	0.7268
DRLSE	1.8132	0.8447	0.5476	**0.6852**	0.6057	0.7203	0.7332
LAC	2.5671	0.8543	0.5855	0.5587	**0.6411**	0.6764	0.7614
MAC	1.8967	0.8507	0.5586	0.6763	0.6097	**0.7265**	0.7358
LSFCM	2.6341	0.8473	0.5876	0.5473	0.6234	0.6726	**0.7643**

Table 23
$DICE_{30}$ for the tested methods for varying Gaussian smoothing. US images type 4.

Model	σ_{best}	Average $DICE$, WP	Average $DICE$, ADF	Average $DICE$, DRLSE	Average $DICE$, LAC	Average $DICE$, MAC	Average $DICE$, LSFCM
WP	2.2269	**0.8882**	0.3847	0.5982	0.3894	0.6137	0.7469
ADF	4.2313	0.6847	**0.5163**	0.3272	0.3058	0.5302	0.7208
DRLSE	1.9146	0.8528	0.3462	**0.6654**	0.3612	0.6389	0.7357
LAC	2.6088	0.8488	0.4112	0.5327	**0.4211**	0.6102	0.7627
MAC	1.9631	0.8559	0.3558	0.6584	0.3683	**0.6413**	0.7381
LSFCM	2.6341	0.8488	0.4137	0.5286	0.4127	0.6087	**0.7643**

Fig. 15. Average computational speed for the US images, Type 1.

obtained by the competing methods with the same σ. For instance, Table 22 shows that for $\sigma_{\text{best,DRLSE}} = 1.8132$, $DICE_{DRLSE} = 0.6852$ but ADF produces $DICE_{ADF} = 0.5476$ with this particular σ.

Clearly, the edge detection routine impacts every method. Moreover, an edge map suitable for one method may not work for another.

However, WP is less sensitive to the edge map and produces $DICE_{WP} \geq 0.8$ for *every edge map*, except the large $\sigma_{ADF,best} = 3.9765$ and $\sigma_{ADF,best} = 4.2313$ required for ADF. Excessive smoothing is detrimental for WP. When large parts of the boundary are lost, the repair balls cannot restore them. However, WP shows the best results for every σ_{best}. Therefore, from a software development viewpoint, WP can replace every method without modifying the preprocessing stage. Our experiments show that to maintain $DICE \geq 0.8$, σ_{WP} must belong to [1.15, 3.1], whereas to maintain $DICE_{WP} \geq 0.7$, σ_{WP} must belong to [0.4274, 3.7524]. A stable and relatively good performance of LSFCM should also be noted. To maintain $DICE_{LSFCM} \geq 0.7$, we need $\sigma_{LSFCM} \in [1.3, 4.6]$. This interval is actually larger than that needed for WP. However, for these test images, $DICE_{LSFCM}$ never reaches 0.8.

Experiment 4. Computational time

Let us now compare the methods in terms of their computational time. The algorithms have been implemented in C++ in a UNIX environment using an Intel(R) Core (TM) i7-6700HQ CPU @ 2.60 GHz with 8 GB RAM. The graphic output was suppressed during the experiments. Since the images have a different size, the speed was

measured in s/pixel. The number of particles is 80% of the number of the image pixels, $\Delta s = 0.0005$ (Section 3.1.2). The WP is the fastest method for Type 1 with an average speed of about 0.00013 s/pixel. For instance, an image with 400×400 pixels is processed in 20 s. For types 2–4, WP are slightly slower than LSFCM and DRLSE, and for types 1 and 3, WP are faster (see Figs. 16–18).

To be fair to WP, the computational time for the competing methods includes cases when the contour totally collapses, which happens fast. That is why WP are slightly slower on types 2–4 that are characterized by broken boundaries. Therefore, given the superior accuracy of the WP and a comparable speed in the range of 10–20 s per image, the efficiency of the WP is outstanding.

Table 24 presents the basic parameters of the model used for segmentation of this series of the US images. The parameters were kept unchanged, regardless of the type of the image, its size, and the edge map quality (see Fig. 18).
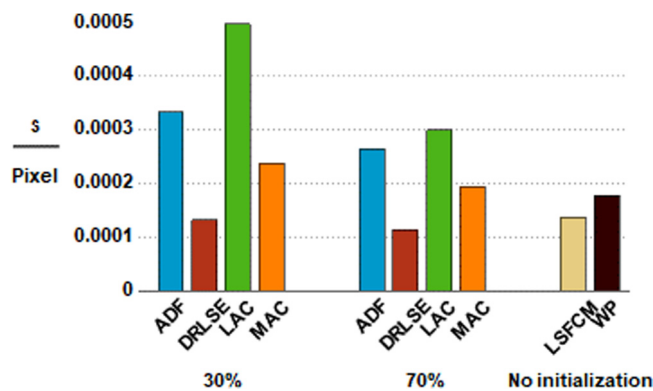

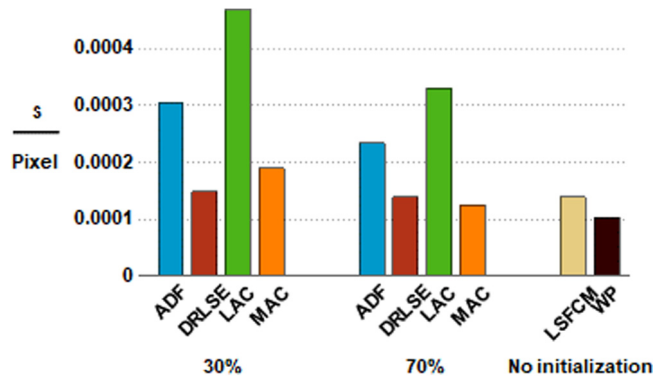**Fig. 16.** Average computational speed for the US images, Type 2.

Fig. 17. Average computational speed for the US images, Type 3.

Table 24
Parameters of WP model for the tested US images.

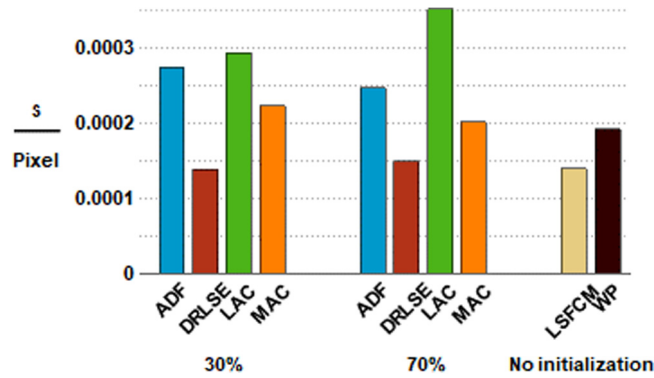| Parameters of the infection sigma-function (Section 3.1.2)			Increment of the edge score (Section 3.1.2)	Time frame to evaluate the average edge score (Section 3.1.2)	Coefficient to define the neighborhood of the repair ball (Section 4.1)	Threshold on the small edge score (Section 4.1)
α	β	δ'	Δs	w	α_k	s_{small}
0.85	0.75	0.9	0.0005	10	1.5	0.5

Fig. 18. Average computational speed for the US images, Type 4.

6. Conclusions

A model based on a new principle of bouncing, multiple walking particles has been proposed and applied to the segmentation of abnormalities in US breast images. For strong noise and broken boundaries, WP outperform recent methods as applied to a large series of US images. Moreover, the model outperforms selected state-of-art methods when the competing methods "know" the ground truth and can adapt the control parameters.

For WP, the average DICE coefficient is approximately 0.9, and the average Hausdorff distance is from 2.5 to 5 pixels for every category of images. The accuracy is always higher than that produced by the reference methods. In many cases, the advantage in accuracy of WP is as high as 100%.

The computational speed is in general higher. Only in a few cases the speed is slightly lower. The reason for that is that the statistics include "failed cases" (collapsed snakes, etc.) which usually require less computational time than the successful segmentations.

Acknowledgments

References

[1] MathWorks File Exchange, Adaptive Diffusion Flow Active Contours for Image Segmentation, https://www.mathworks.com/matlabc entral/fileexchange/42435-adaptive-diffusion-flow-active-contours-for-image-segmentation?focused=3789006&tab=function. (Accessed 8 May 2019).

[2] MathWorks, Level set for image segmentation, https://www.mathworks.com/matlabcentral/fileexchange/12711-level-set-for-image-segm entation. (Accessed 10 May 2019).

[3] MathWorks, Localized Active Contour, https://uk.mathworks.com/matlabcentral/fileexchange/44906-localized-active-contour. (Accessed 10 March 2019).

[4] MathWorks, Spatial Fuzzy Clustering and Level Set Segmentation, https://www.mathworks.com/matlabcentral/fileexchange/31068-spati al-fuzzy-clustering-and-level-set-segmentation. (Accessed 21 May 2019).

[5] GitHub, bus-segmentation, https://github.com/mawady/bu-segmentation. (Accessed 17 May 2019).

[6] MathWorks, Active contour without edge, https://www.mathworks.com/matlabcentral/fileexchange/34548-active-contour-without-edge. (Accessed 1 June 2019).

[7] Y.S. Akgul, C. Kambhamettu, M. Stone, Extraction and tracking of the tongue surface from ultrasound image sequences, Proc. IEEE Comput. Soc. Conf. Comput. Vis. Pattern Recognit. (1998) 298–303.

[8] S. Benmazou, S. Layachi, F.M. Hayet, Segmentation of images based cellular automata-reactive agent implemented in netlogo platform, Int. J. Comput. Appl. 45 (2012) 40–43.

[9] T. Brox, D. Cremers, On the statistical interpretation of the piecewise smooth Mumford–Shah functional, in: Proceedings of SSVM, 2007, pp. 203–213.

[10] Q. Cai, H. Liu, S. Zhou, J. Sun, J. Li, An adaptive-scale active contour model for inhomogeneous image segmentation and bias field estimation, Pattern Recognit. 82 (2018) 79–93.

[11] V. Caselles, R. Kimmel, G. Sapiro, A geometric model for active contours, Int. J. Comput. Vis. 22 (1) (1997) 61–79.

[12] T.F. Chan, L.A. Vese, Active contours without edges, IEEE Trans. Image Process. 10 (2) (2001) 266–277.

[13] J. Cheng, S.W. Foo, Dynamic directional gradient vector flow for snakes, IEEE Trans. Image Process. 15 (6) (2006) 1563–1571.

[14] H.D. Chenga, J. Shana, W. Jua, Y. Guoa, L. Zhang, Automated breast cancer detection and classification using ultrasound images: A survey, Pattern Recognit. 43 (2010) 299–317.

[15] V. Chinnadurai, G. Damayanti Chandrashekhar, Neuro-level set system based segmentation in dynamic susceptibility contrast enhanced and diffusion weighted magnetic resonance images, Pattern Recognit. 45 (9) (2012) 3501–3511.

[16] M. Chitsaz, W.C. Seng, Medical image segmentation using a multi-agent system approach, Int. Arab J. Inf. Technol. 10 (3) (2013) 222–229.

[17] CodeForge, Sourcecodes, GVF snake procedures for image segmentation using MATLAB language, 2019, http://www.codeforge.com/read/159797/NGVF.m__html. (Accessed 8 June 2019).

[18] D.J. Doshi, D.E. March, G.M. Crisi, B.F. Coughlin, Complex cystic breast masses: diagnostic approach and imaging-pathologic correlation, Radiographics 27 (2007) 53–64.

[19] E. Duchesnay, Agents situés dans l'image et organisés en pyramide irrégulière: contribution à la segmentation par une approche d'agrégation coopérative et adaptative (Ph.D. thesis), Université Rennes-1, 2001.

[20] V. Estellers, D. Zosso, R. Lai, S. Osher, J.P. Thiran, X. Bresson, Efficient algorithm for level set method preserving distance function, IEEE Trans. Image Process. 21 (12) (2011) 4722–4734.

[21] K. Fergani, D. Lui, C. Scharfenberger, A. Wong, D.A. Clausi, Hybrid structural and texture distinctiveness vector field convolution for region segmentation, Comput. Vis. Image Underst. 125 (2014) 85–96.

[22] G. Gao, C. Wen, H. Wang, Fast and robust image segmentation with active contours and Student's-t mixture model, Pattern Recognit. 63 (2017) 71–86.

[23] L. Germond, M. Dojat, C. Taylor, C. Garbay, A cooperative framework for segmentation of MRI brain scans, Artif. Intell. Med. 20 (2000) 77–93.

[24] Github, 2019,

[25] C.L. Guyader, L. Guillot, Extrapolation of vector fields using the infinity Laplacian and with application to image segmentation, Commun. Math. Sci. 7 (2) (2009) 423–452.

[26] K. Hosch M.L. Giger, L. Venta, C.J. Vyborny, Computerized diagnosis of breast lesions on ultrasound, Med. Phys. 29 (2) (2002) 157–164.

[27] Q. Huang, Y. Luo, Q. Zhang, Breast ultrasound segmentation: a survey, Int. J. Comput. Assist. Radiol. Surg. 12 (2017) 493.

[28] A.C. Jalba, M.H.F. Wilkinson, J.B.T.M. Roerdink, Automatic image segmentation using a deformable model based on charged particles, Lecture Notes in Comput. Sci. 3211 (2004) 1–8.

[29] N. Jifeng, W. Chengke, L. Shigang, Y. Shuqin, NGVF: an improved external force field for active contour model, Pattern Recognit. Lett. 28 (1) (2007) 58–63.

[30] I.S. Jung, D. Thapa, G.N. Wang, Automatic Segmentation and Diagnosis of Breast Lesions Using Morphology Method Based on Ultrasound, in: Lect. Notes Artif. Intell (Subseries Lect. Notes Comput. Sci.), vol. 3614, 2005, pp. 1079–1088.

[31] H. Kagawa, M. Kinouchi, M. Hagiwara, Image segmentation by artificial life approach using autonomous agents, in: Neural Networks, IJCNN'99, Int. Jt. Conf., Vol. 6, 1999, pp. 4413–4418.

[32] M. Kass, A. Witkin, D. Terzopoulos, Snakes: Active contour models, Int. J. Comput. Vis. 1 (4) (1988) 321–331.

[33] C. Keatmanee, U. Chaumrattanakul, K. Kotani, S.S. Makhanov, Initialization of active contours for segmentation of breast cancer via fusion of ultrasound, Doppler, and elasticity images, Ultrasonics (2018) (in print).

[34] K. Kirimasthong, A. Rodtook, U. Chaumrattanakul, S.S. Makhanov, Phase portrait analysis for automatic initialization of multiple snakes for segmentation of the ultrasound images of breast cancer, Pattern Anal. Appl. 20 (2017) 239–251.

[35] S. Lankton, A. Tannenbaum, Localizing region-based active contours, IEEE Trans. Image Process. 17 (11) (2008) 2029–2039.

[36] B. Li, S.T. Acton, Active contour external force using vector field convolution for image segmentation, IEEE Trans. Image Process. 16 (8) (2007) 2096–2106.

[37] B. Li, S.T. Acton, Automatic active model initialization via Poisson inverse gradient, IEEE Trans. Image Process. 17 (8) (2008) 1406–1420.

[38] B.N. Li, C.K. Chui, S. Chang, S.H. Ong, Integrating spatial fuzzy clustering with level set methods for automated medical image segmentation, Comput. Biol. Med. 41 (2011) 1–10.

[39] C. Li, C. Kao, J.C. Gore, Z. Ding, Implicit active contours driven by local binary fitting energy, in: Proceedings of IEEE Conference on Computer Vision and Pattern Recognition, 2007, pp. 1–7.

[40] C. Li, J. Liu, M.D. Fox, Segmentation of external force field for automatic initialization and splitting of snakes, Pattern Recognit. 38 (11) (2005) 1947–1960.

[41] C. Li, C. Xu, C. Gui, M.D. Fox, Level set evolution without re-initialization: a new variational formulation, IEEE Comput. Soc. Conf. Comput. Vis. Pattern Recognit. 1 (2005) 430–436.

[42] C. Li, C. Xu, C. Gui, M.D. Fox, Distance regularized level set evolution and its application to image segmentation, IEEE Trans. Image Process. 19 (12) (2010) 3243–3254.

[43] C. Liu, W. Liu, W. Xing, An improved edge-based level set method combining local regional fitting information for noisy image segmentation, Signal Process. 130 (2017) 12–21.

[44] S. Liu, Y. Peng, A local region-based Chan–Vese model for image segmentation, Pattern Recognit. 45 (7) (2012) 2769–2779.

[45] W. Liu, Y. Shang, X. Yang, Active contour model driven by local histogram fitting energy, Pattern Recognit. Lett. 34 (2013) 655–662.

[46] J. Liu, Y.Y. Tang, Adaptive image segmentation with distributed behavior-based agents, IEEE Trans. Pattern Anal. Mach. Intell. 21 (1999) 544–551.

[47] J. Liu, Y. Tang, Y. Cao, An evolutionary autonomous agents approach to image feature extraction, IEEE Trans. Evol. Comput. 1 (2) (1997) 141–158.

[48] Z. Ma, J.M.R.S Tavares, A novel approach to segment skin lesions in dermoscopic images based on a deformable model, IEEE J. Biomed. Health Inf. 20 (2016) 615–623.

[49] Z. Ma, J.M.R.S. Tavares, R.N. Jorge, A review on the current segmentation algorithms for medical images, in: Proceedings of the First International Conference on Computer Imaging Theory and Applications, Lisboa, Portugal, February 5–8, 2009.

[50] A. Madabhushi, D.N. Metaxas, Combining low- high-level and empirical domain knowledge for automated segmentation of ultrasonic breast lesions, IEEE Trans. Med. Imaging 22 (2) (2003) 155–169.

[51] P. Márquez-Neila, L. Baumela, L. Alvarez, A morphological approach to curvature-based evolution of curves and surfaces, IEEE Trans. Pattern Anal. Mach. Intell. 36 (2014) 2–17.

[52] S. Mazouzi, Z. Guessoum, F. Michel, M. Batouche, An agent-based approach for range image segmentation, in: N. Jamali, P. Scerri, T. Sugawara (Eds.), Massively Multi-Agent Technology, AAMAS 2007, Lecture Notes in Computer Science, vol. 5043, Springer, Berlin, Heidelberg.

[53] H. Min, W. Jia, X.-F. Wang, Y. Zhao, R.-X. Hu, Y.-T. Luo, F. Xue, J.-T. Lu, An intensity-texture model based level set method for image segmentation, Pattern Recognit. 48 (2015) 1547–1562.

[54] D. Mumford, J. Shah, Optimal approximations by piecewise smooth functions and associated variational problems, Comm. Pure Appl. Math. 42 (5) (1989) 577–685.

[55] S. Niu, Q. Chen, L. de Sisternes, Z. Ji, Z. Zhou, D.L. Rubin, Robust noise region-based active contour model via local similarity factor for image segmentation, Pattern Recognit. 61 (2017) 104–119.

[56] S. Osher, J.A. Sethian, Fronts propagating with curvature-dependent speed: algorithms based on Hamilton–Jacobi formulations, J. Comput. Phys. 79 (1988) 12–49.

[57] P. Perona, J. Malik, Scale space and edge detection using anisotropic diffusion, IEEE Trans. Pattern Anal. Mach. Intell. 12 (1990) 629–639.

[58] Z. Ren, Adaptive active contour model driven by fractional order fitting energy, Signal Process. 117 (2015) 138–150.

[59] N. Richard, M. Dojat, C. Garbay, Automated segmentation of human brain MR images using a multi-agent approach, Artif. Intell. Med. 30 (2004) 153–175.

[60] A. Rodtook, K. Kirimasthong, W. Lohitvisate, S.S. Makhanov, Automatic initialization of active contours and level set method in ultrasound images of breast abnormalities, Pattern Recognit. 79 (2018) 172–182.

[61] A. Rodtook, S.S. Makhanov, Multi-feature gradient vector flow snakes for adaptive segmentation of the ultrasound images of breast cancer, J. Vis. Commun. Image Represent. 24 (8) (2013) 1414–1430.

[62] S. Selvan, S. Shenbagadevi, Automatic seed point selection in ultrasound echography images of breast using texture features, Biocybernetics Biomed. Eng. 35 (3) (2015) 157–168.

[63] A.A. Taha, A. Hanbury, Metrics for evaluating 3D medical image segmentation: Analysis, selection, and tool, BMC Med. Imaging (2015) 15–29.

[64] J. Tang, A multi-direction GVF snake for the segmentation of skin cancer images, Pattern Recognit. 42 (6) (2009) 1172–1179.

[65] C. Tauber, H. Batatia, A. Ayache, A general Quasi-automatic initialization for snakes application to ultrasound images, in: Proceedings of the International Conference on Image Processing, Vol. 2, IEEE Internat., 2005, pp. 806–809.

[66] C. Tauber, H. Batatia, A. Ayache, Quasi-automatic initialization for parametric active contours, Pattern Recognit. Lett. 31 (1) (2010) 83–90.

[67] A. Tsai, A. Yezzi, A.S. Willsky, Curve evolution implementation of the Mumford–Shah functional for image segmentation, denosing, interpolation, and magnification, IEEE Trans. Image Process. 10 (8) (2001) 1169–1186.

[68] Y. Wang, Y. Jia, L. Liu, Harmonic gradient vector flow external force for snake model, Electron. Lett. 44 (2) (2008) 105–106.

[69] Y. Wang, J. Liang, Y. Jia, On the critical point of gradient vector flow snake, in: ACCV2007, in: LNCS, vol. 4844, 2007, pp. 754–763.

[70] M. Wei, Y. Zhou, M. Wan, A fast snake model based on non-linear diffusion for medical image segmentation, Comput. Med. Imaging Graph. 28 (3) (2004) 109–117.

[71] Y. Wong, P.C. Yuen, C.S. Tong, Segmented snake for contour detection, Pattern Recognit. Lett. 31 (11) (1998) 1669–1679.

[72] Y. Wu, Y. Wang, Y. Jia, Adaptive diffusion flow active contours for image segmentation, Comput. Vis. Image Underst. 117 (10) (2013) 1421–1435.

[73] M. Xian, Y. Zhang, H.D. Cheng, F. Xu, B. Zhang, J. Ding, Automatic breast ultrasound segmentation: A survey, Pattern Recognit. 79 (2018) 340–355.

[74] G. Xingfei, T. Jie, An automatic active contour model for multiple objects, in: Proc. Internat. Conf. Pattern Recognit., Vol. 2, 2002, pp. 881–884.

[75] C. Xu, J.L. Prince, Generalized gradient vector flow external forces for active contours, Signal Process. 71 (2) (1998) 131–139.

[76] C. Xu, J.L. Prince, Snake and gradient vector flow, IEEE Trans. Image Process. 7 (3) (1998) 359–369.

[77] X. Yang, X. Gao, D. Tao, X. Li, Improving level set method for fast auroral oval segmentation, IEEE Trans. Image Process. 23 (7) (2014) 2854–2965.

[78] X. Yuan, N. Situ, G. Zouridakis, A narrow band graph partitioning method for skin lesion segmentation, Pattern Recognit. 42 (6) (2009) 1017–1028.

[79] X.-H. Zhi, H.-B. Shen, Saliency driven region-edge-based top down level set evolution reveals the asynchronous focus in image segmentation, Pattern Recognit. 80 (2018) 241–255.